

Article

# Interactions between Hydrodynamic Forcing, Suspended Sediment Transport, and Morphology in a Microtidal Intermediate-Dissipative Beach

Anlly Melissa Guerrero <sup>1,\*</sup> , Luis Otero <sup>1</sup> , Silvio Ospino <sup>1</sup> and Jairo Cueto <sup>2,3</sup> 

<sup>1</sup> Geociencias-GEO4 Research Group, Department of Physics and Geosciences, Universidad del Norte, Km 5 vía Puerto Colombia, Barranquilla 081007, Colombia; ljotero@uninorte.edu.co (L.O.); osilvio@uninorte.edu.co (S.O.)

<sup>2</sup> Coastal Geology and Sedimentology Group, Institute of Geosciences, Kiel University, 24118 Kiel, Germany; jairo.cueto@ifg.uni-kiel.de

<sup>3</sup> Research Group in Natural and Exact Sciences—GICNEX, Department of Natural and Exact Sciences, Universidad de la Costa, Barranquilla 081007, Colombia

\* Correspondence: anllyg@uninorte.edu.co

**Abstract:** This study aims to investigate the hydrodynamic-morphological interactions on a microtidal intermediate-dissipative beach under low to moderate wave energy conditions using field measurements during two climatic seasons. The separate contributions of currents, sea-swell waves, and infragravity waves to high- and low-frequency sediment fluxes were analyzed. The infragravity wave energy was more relevant near the swash zone than in other areas. Although the currents are the primary suspended sediment transport mechanism, the results suggest that the waves are an important driver of sediment suspension from the seabed. The results indicate that Sea-Swell (SS) waves and cross-shore currents are the prevailing hydrodynamic factors in nearshore sediment transport, and the cross-shore suspended sediment transport rates are higher than those in along-shore transport. The submerged bar intensified during the wet season (1–4 November 2018) when the wave height intensities were lower, contrary to the dry season (24–25 March 2018). Significant accretion nearshore was identified (in the subaerial beach) during the wet season when the suspended sediments were greater, the SS-wave heights nearshore were lower, and sediment flux was directed onshore. A notorious erosion was distinguished during the dry season. The most representative volume changes occurred during the dry season (with high erosion), which is attributed to the high SS-wave energy.

**Keywords:** morphodynamics; hydrodynamics; suspended sediment transport; acoustic backscatter; intermediate-dissipative beach; microtidal beach



**Citation:** Guerrero, A.M.; Otero, L.; Ospino, S.; Cueto, J. Interactions between Hydrodynamic Forcing, Suspended Sediment Transport, and Morphology in a Microtidal Intermediate-Dissipative Beach. *J. Mar. Sci. Eng.* **2024**, *12*, 1141. <https://doi.org/10.3390/jmse12071141>

Academic Editor: Abdellatif Ouahsine

Received: 13 June 2024

Revised: 30 June 2024

Accepted: 2 July 2024

Published: 6 July 2024



**Copyright:** © 2024 by the authors. Licensee MDPI, Basel, Switzerland. This article is an open access article distributed under the terms and conditions of the Creative Commons Attribution (CC BY) license (<https://creativecommons.org/licenses/by/4.0/>).

## 1. Introduction

Seasonally dominated coastal zones exhibit two cycles of beach morphological change [1]. The first cycle is related to pre- and post-storm evolution, with the fastest, most drastic changes occurring on the shoreline. The second cycle is seasonal, associated with winter/summer morphological change. Seasonal changes occur more frequently than those caused by waves in extreme conditions. Differentiating morphological changes associated with both cycles is essential for understanding morphodynamic behavior on a coastal beach along a short-term cycle. This understanding, in turn, allows for mitigation of possible seasonal impacts on a beach, e.g., coastal erosion processes influenced by sediment redistribution or by transitions between contrasting climate seasons.

Sediment transport on beaches has been a topic of scientific interest since the mid-20th century [2]. The morphodynamic approach, initially formalized by [3] and later adopted by [1,4,5] for the study of beaches, involves the interactions between fluid dynamics,

sediment movement, and morphology. Studies on beach morphodynamics are challenging due to the synchronous occurrence between hydrodynamic forces and sediment transport. In addition, measurements are difficult due to the complex logistics required in the high turbulence environments of the inner surf zone [6,7].

Previous research showed that Sea-Swell (SS) waves were the main mechanism for sand suspension, whereas Infragravity waves (IG) would transport the sediment through advection [8,9]. So, the sediment flux distribution due to SS-wave and IG-wave is herein analyzed separately. Using these variables independently allows us to understand suspended sediment transport influenced by high-frequency and low-frequency wave movements, as well as their effect on sediment redistribution at the subaerial beach. The microtidal dissipative beaches with a moderate slope and microtidal regime are particularly sensitive to seasonal variations and changes in oceanographic conditions, significantly contributing to sediment distribution, coastal bar formation, and shoreline configuration [9–11]. The suspended sediment fluxes were estimated from the current velocity and suspended sediment concentration profiles divided by short- and long-wave contributions. This information allows us to assess sediment flux direction as well as beach responses to short-term seasonal variations.

The Caribbean coastline of Colombia spans over 1750 km, encompassing approximately 54.86% of the total coastline. The remaining 45.14% of the Colombian coastline is comprised of 1448 km of macrotidal Pacific coasts [12]. Despite the large extent of its coastline, most studies of beach morphological change on the Caribbean coast of Colombia have focused mostly on extreme events (e.g., hurricanes, cyclones, cold fronts, tsunamis), whereas moderate- to low-energy wave conditions remain poorly assessed. The latter conditions are often disregarded in analyses because of their less drastic and sudden behavior; nevertheless, focusing only on extreme events leads to an incomplete comprehension of evolution processes. Furthermore, it is important to delve deeper into moderate wave conditions, which occur with greater frequency and play a critical role in beach configuration and stability. Therefore, this research will be based on studying the morphological change of a microtidal intermediate-dissipative beach under low-to moderate-energy conditions in two contrasting climate seasons. This study is relevant for understanding the morphological processes along the Colombian coast because it identified short-term and medium-term change patterns, as well as erosion and deposition of sediment from a seasonal analysis. Lastly, the results of this research could be used as tools for coastal management, conservation, and adaptation strategies for coastal erosion processes.

In this study, morphological evolution will be analyzed on a microtidal intermediate-dissipative beach by collecting in-situ data during two contrasting climatic seasons. Here, it is considered that intermediate beach states exhibit strong morphodynamic feedback, with locally significant transport rates and steep transport gradients [13]. Several parameters were assessed in the most dynamic zone of the beach (between the surf zone and near the swash zone). These parameters include sea level variation, wave height, local current magnitude and direction, initial morphological conditions, sediment grain size, depth, and turbidity. The results of this study highlight how field data from the surf zone, particularly those near the swash zone, are essential for the qualitative and quantitative determination of sediment transport on beaches.

This research aims to describe the continuous interaction between waves (both SS and IG), tides, currents, and suspended sediment transport through: (1) the spatiotemporal evolution of cross-shore hydrodynamic forcing and suspended sediment concentration; (2) cross-shore sediment fluxes; and (3) the relationship between hydrodynamics and beach volumetric changes (e.g., erosion/accretion zones and submerged bar migration). This study will analyze the most significant seasonal variations as well as the sedimentary dynamics present in a microtidal intermediate-dissipative beach. Long-term morphological changes, or those caused by high energy events such as cold fronts or rough sea conditions, among others, will not be discussed herein, as this type of phenomenon did not occur during the measurement's days.

## 2. Materials and Methods

### 2.1. Study Area

This study was performed at Bocatocino Beach, Juan de Acosta municipality, Atlántico Department, Colombia (Figure 1a). Bocatocino Beach exhibits a micro-tidal regime typical of the Caribbean coastline of Colombia, with a range of 0.48 m [14,15]. The wave climate in the proximal marine zone and coastal platform of the Colombian Caribbean, including Bocatocino Beach, is dominated by waves coming from the NE and NNE, with a probability of occurrence of 82% and 12%, respectively [15,16]. Bocatocino Beach has an intermediate-dissipative profile (Figure 1e), with a steep slope in the emerging part of the beach (average slope  $\beta \approx 0.134$ ). The slope becomes gentler in the submerged section, with an almost constant value of 0.014 up to 134 m away from the coast, where it becomes slightly steeper ( $\beta \approx 0.018$ ). Coarse sand is the predominant sediment at Bocatocino Beach (see Section 2.3).

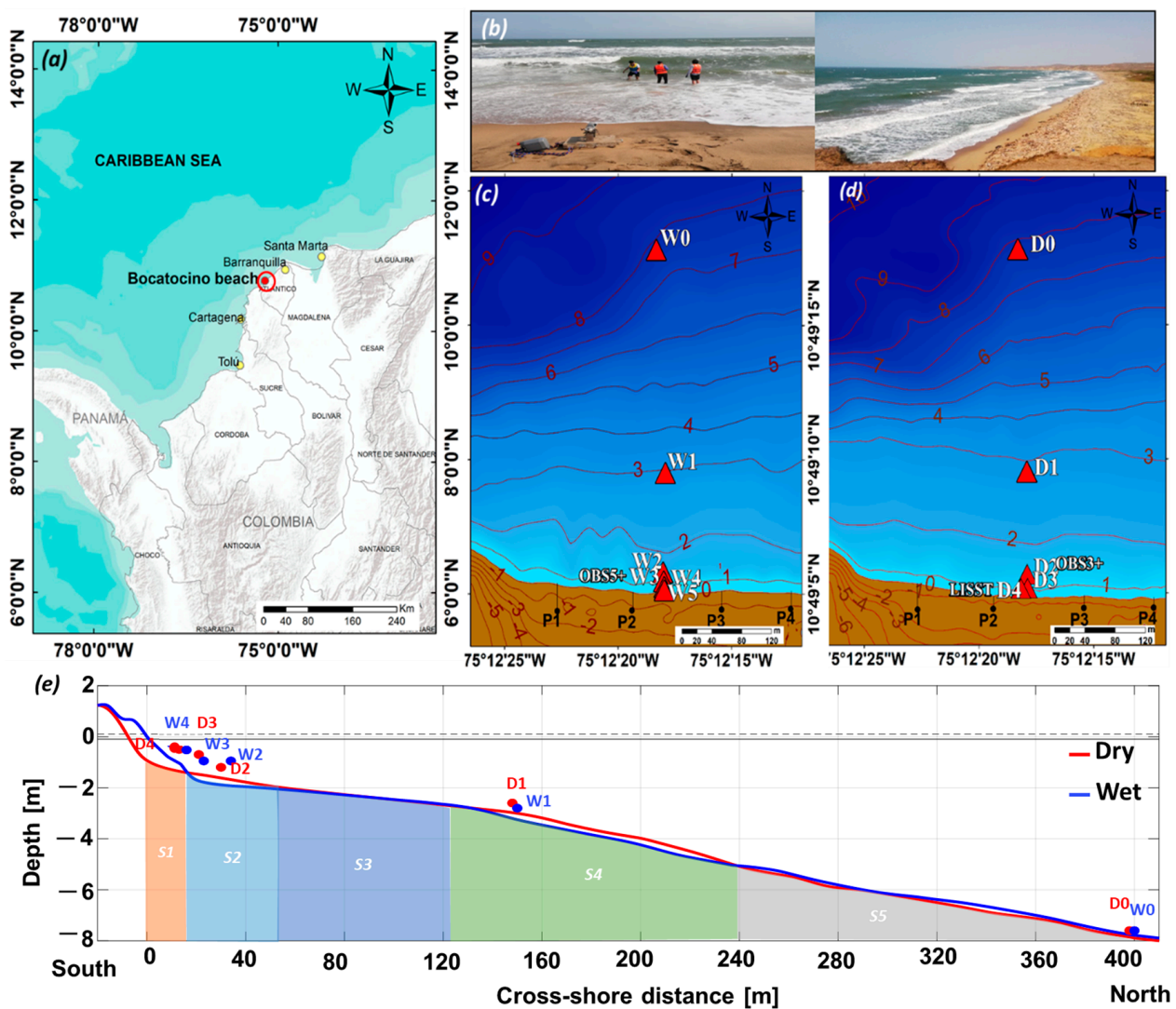


**Figure 1.** (a) Regional location of the study area; (b) Bocatocino beach during the measurement days; (c) Bathymetric data of 1 November, 2018 and the location of profiles P1, P2, P3, and P4 from 1 to 4 November, 2018 (Wet season), (d) Bathymetric data from 24 to 25 March 2019 and the location of profiles P1, P2, P3, and P4 from 24 to 25 March 2019 (Dry season), (e) Topo-bathymetric profiles for the wet season (blue line) and the dry season (red line). The sensor with the letter W corresponds to the equipment installed in the wet season, and D corresponds to the equipment in the dry season. In addition, the profiles were divided into 5 sections (S1, S2, S3, S4, and S5).

The weather and wave regime in the study area is influenced by the migration of the Intertropical Convergence Zone (ITCZ), where Northeast (NE) and Southeast (SE) trade winds converge [15]. Due to the double passage of the ITCZ over the Colombian Caribbean Sea, this region has two dry seasons (December–March and June–July) and two wet seasons (April–May and August–November) [17,18]. Dry seasons are characterized by high-speed winds from the Northeast [15]. The largest waves occur during these seasons, with an average significant height (Hs) of 2.3 m [19]. On the other hand, wet seasons feature higher precipitation levels and lower wind speeds from the East [20], with an average Hs of 1.1 m.

### 2.2. Field Experiments

Field experiments were performed to compile hydrodynamic and topo-bathymetric data from Bocatocino Beach during the dry and wet seasons. The first field experiment was performed in the wet season, from 1 to 4 November 2018. The second experiment was performed during the dry season, between 22 and 25 March 2019.

Water level data were collected with pressure sensors (RBR duo and RBR). Flow rates were collected with current meters (Aquadopp® Profiler, Nortek group, Boston, MA, USA). On the other hand, suspended sediment concentration (SSC) was measured with turbidity sensors (OBS-3+ and OBS-5+, Campbell Scientific, Barcelona, España). In addition, volume concentration data was determined for 36 sediment size classes (LISST-200X, Sequoia, Bellevue, WA, USA). Sensors were installed cross-shore on Bocatocino Beach (Figure 1c,d). The experimental setup allowed for the analysis of the hydrodynamic spatio-temporal evolution of nearshore hydrodynamics as well as the transformation of associated SS-waves along the shoaling zone, surf zone, and near the swash zone (Table 1).

**Table 1.** Instrument configuration for the dry and wet seasons at Bocatocino Beach. Note: The acronym HR means high resolution.

Season	Sensor/ Symbology	Instrument	Location	Distance from the Coast [m]	Depth [m]
Wet	W0	Nortek Aquadopp Profiler	Shoaling zone	400	~7.9
	W1	Nortek Aquadopp Profiler	Breaking zone	150	~2.8
	W2	Nortek Aquadopp Profiler		34	~1.3
	W3 and OBS 5+	Nortek Aquadopp Profiler HR and OBS5+	Surf zone	23	~1.2
	W4	Nortek Aquadopp Profiler HR		16	~1.1
	W5	RBR	Near the Swash zone	10	~1.0
Dry	D0	RBR	Shoaling zone	400	~7.9
	D1	Nortek Aquadopp Profiler	Breaking zone	150	~2.8
	D2 and OSB 3+	Nortek Aquadopp Profiler and OBS3+	Surf zone	30	~1.4
	D3	Nortek Aquadopp Profiler HR		21	~1.3
	D4 and LISST	Nortek Aquadopp Profiler HR and LISST	Near the Swash zone	13	~1.1

Pressure sensors, current measurers, OBS3+ sensors, and LISST sensors were configured to measure at a frequency of 5 Hz during the dry season. The D0 sensor was an RBR instrument located 400 m away from the shoreline. D1 and D2 sensors were configured at a vertical resolution of 50 cells and widths of 20 and 10 cm, respectively. Sensors D3 and D4 were configured at a vertical resolution of 28 cells and 1 cm of width. The blanking distance for sensors D1, D2, D3, and D4 was 10 cm.

Regarding topographic information, beach profile measurements were carried out from 1 to 4 November 2018 for the wet season, and from 24 and 25 March 2019 for the dry season. Beach profiles were measured using a total station with an accuracy of  $\pm 0.0762$  m for the combined x and y coordinates and  $\pm 0.0762$  m for the z coordinate. The data were georeferenced through a differential global positioning system. Four profiles were established cross-shore, strategically distributed along the hydrodynamic array. The beach profiles P1 to P2 were located along the coast (Figure 1c,d). To collect depth data, bathymetric surveys were carried out for each climatic season using a digital echo sounder, and a high-frequency (200 kHz) transducer with an accuracy of  $0.01 \text{ m} \pm 0.1\%$  depth was used. Depth data were taken from high and low tide forecasts published by the Colombian Institute of Hydrology, Meteorology, and Environmental Studies, IDEAM [21], and were referenced to the mean low water springs (MLWS). Hydrodynamic, topographic, and bathymetric measurements will determine the relationship between hydrodynamic forcing (e.g., SS and IG waves, long-shore and cross-shore currents, sea level, wave steepness) and coast morphological changes.

### 2.3. Sedimentology Analysis

Three sediment samples were collected in both climatic seasons in order to determine the sedimentological characteristics of the study area. Three points of interest (in the surf zone) were chosen for sample collection. Sediment samples were analyzed to characterize the composition, textural group, and grain size of each coastal zone through the GRADIS-TAT tool proposed by [22]. Table 2 shows the composition percentages and textural groups of six sediment samples collected for both climatic seasons.

**Table 2.** Composition percentages and the textural group for six (6) sedimentological samples according to each nearshore littoral zone from which they were extracted.

Climatic Season	Sample	Coastal Zone	Textural Group	Very Fine Sand (%)	Fine Sand (%)	Medium Sand (%)	Coarse Sand (%)	Very Coarse Sand (%)	Gravel (%)
Wet	1	Surf zone	Slightly gravelly sand	0.8	12.3	27.1	47.7	10.7	1.4
	2	Near the swash zone	Sandy gravel	0.4	3.1	5	23.9	30.1	37.5
	3	Subaerial zone	Slightly gravelly sand	1.0	24.6	51.7	20.4	2.1	0.2
Dry	4	Surf zone	Gravelly sand	0.2	3.1	18.7	36.5	20.0	21.5
	5	Near the swash zone	Sandy gravel	0.1	0.7	9.8	34.6	22.3	32
	6	Subaerial zone	Slightly gravelly sand	0.7	9.5	52.5	33.8	3.3	0.2

### 2.4. Data Series Processing

A quality control protocol, comprising a visual inspection process and the implementation of a manual quality control tool, was applied to the raw field data series. In the visual inspection stage, unusual patterns or fluctuations, such as extreme, outlier, or null values, were identified. These unusual values may be caused by external conditions, such as the presence of swimmers in small vessels near the measuring site. These outliers were removed from the dataset. Measure data near or above the sea surface were eliminated due to the presence of erroneous data caused by contamination of the lateral lobe.

A moving average filter was used as a quality control tool, applying a sliding window to the data series to identify anomalous values and correct atypical values if needed. The sliding window was relatively small (approximately between 5 and 20 s), given the frequency and nature of data fluctuations. Current, wave, and turbidity data were measured each second for three consecutive days. Therefore, data fluctuations can be rapid and transitory. Nevertheless, this window allowed us to capture short but significant events as atypical data noise was deleted. In some cases, it was necessary to adjust the window size during the analysis. To identify systematic biases in measurements, thresholds where

atypical values were found in the data series were defined using mean (central trend) and standard deviation trends. These statistics play an important role in the validation of measured data as well as in data quality control. Data considered atypical were those outside the range (two or three standard deviations away from the median). Lastly, a Nearest Neighbor Analysis was applied to detect atypical values that remained undetected by previous methods.

Data were analyzed through time-domain representations using Fourier Transform (FFT) and Cross-wavelet Transform (XWT), following previous studies [17,19].

#### 2.4.1. Time and Frequency Domain Processing

Hydrodynamic (e.g., sea level, cross-shore, long-shore currents) and turbidity data taken in field campaigns were split into 1-h sea states to perform time-domain analyses. Fourier transform analysis was employed to estimate the wave energy density ( $S$ ) of the free surface elevation series in the frequency domain. Eight Hamming windows were used, with an overlapping of 50% and a frequency bandwidth of 0.002 Hz. Significant wave heights were classified into two bands: gravity, or SS ( $H_{mo,SS}$ ), and infragravity ( $H_{mo,IG}$ ), using Equation (1) and according to [23].

$$H_{mo,SS} = 4\sqrt{\int_{f_{0.005}}^{f_{split}} S(f) df}, H_{mo,IG} = 4\sqrt{\int_{f_{split}}^{0.5} S(f) df} \quad (1)$$

where a cutoff frequency ( $f_{split}$ ) of 0.05 Hz, approximately equal to half the average peak frequency ( $f_p = 1/T_p$ ) of offshore waves, is used to separate infragravity (IG) and gravity (SS) bands. This choice of cut-off frequency is based on the tendencies of gravity and IG wave energy frequencies in deep water conditions. Most gravity-wave energy displays frequencies  $> f_p/2$ , whereas most IG-wave energy lies at frequencies  $< f_p/2$  [24].

#### 2.4.2. Wave Steepness and Breaking Wave Percentage

Wave steepness was used as a proxy to assess sediment transport and determine the effect of wave conditions on suspended sediment. Wave steepness was calculated using Equation (2):

$$\text{Wave steepness} = H/L^* \quad (2)$$

where  $H$  and  $L^*$  are wave height and wavelength, respectively. The dispersion equation (3) was used to determine wavelength and wave period values [25].

$$L^* = gT^2 \tanh\left(\frac{2\pi h}{L}\right) / 2\pi \quad (3)$$

where  $T$  is wave period,  $h$  is depth, and  $g$  is the gravitational acceleration. In this study, significant wave period ( $T_{sig}$ ) and height ( $H_{sig}$ ) values were used. In a shallow-water approximation, Equation (3) is simplified as:

$$L_{shallow} = T\sqrt{gh} \quad (4)$$

In this study, the breaking wave percentage was calculated following [26] as the ratio between the number of waves classified as broken ( $N_{br}$ ) and the total number of waves ( $N_t$ ) in the same time interval as  $Q_b = N_{br}/N_t$ .

#### 2.4.3. Principal Component Analysis (PCA)

The PCA method was used to determine the correlated variables of multiple hydrodynamic forcing factors with the topographic change. This method has been very useful in coastal research as a tool for assessing the role of meteorological and marine forces on beach morphological change [4,27]. In this work, a PCA was employed between marine forcing (heights  $H_{mo,ss}$ ,  $H_{mo,IG}$ , wave steepness, velocities, and maximum tide level) and the sediment suspended concentration (SSC) to analyze the response of sediment supply

nearshore, which could be a proxy for the topographic change on beaches. Correlations between principal and secondary components were calculated; those with values above 0.47 were considered significant.

#### 2.4.4. Estimated Suspended Sediment Concentration from Acoustic Backscattered (ABS)

The sonar equation was used in this study to quantify SSC, first by converting acoustic echo intensity ( $E$ ), measured in counts by the ADCP, and posteriorly by converting to acoustic backscatter ( $ABS$ ), measured in dB, using the methods provided by [28–30]. Echo retrodispersion in dB is given by [28]:

$$ABS = \{C - L_{DBM} - P_{DBW}\} + 2\alpha R + \left\{10\log_{10} \left[ (T_{TD} + 273.16)R^2 \right] \right\} + \left\{10\log_{10} \left[ 10^{\frac{K_c(E-E_r)}{10}} - 1 \right] \right\} \quad (5)$$

Equation (6) can be rewritten in a simpler form as:

$$ABS = K_c + 2TL' + RL' \quad (6)$$

In the first terms of Equations (5) and (6),  $C$  is an empiric constant,  $L_{DBM}$  is given by  $10\log_{10}(L)$ , with  $L'$  being transmitted pulse length (measured in m), and  $P_{DBW}$  is defined by  $10\log_{10}(P)$ , with  $P$  being transmitted frequency (in watts).  $K_c$  is given as,

$$K_c = \frac{127.3}{T_{TD} + 273^\circ} \quad (7)$$

The second term in Equations (5) and (6) represents a parameter of bidirectional transmission loss ( $2TL'$ ), in which parameter  $\alpha$  is the sound absorption coefficient in water (in dB/m),  $R$  is the range along the acoustic beam (in m), and  $T_{TD}$  is the temperature at the depth of the transducer (in °C).

$R$  was calculated following by [29,31], as follows:

$$R = z / \cos(\text{beam angle}, 25^\circ \text{ for Aquadopp/AWAC}) \quad (8)$$

$\alpha$  was calculated using the formula provided [32], as follows:

$$\alpha = 0.106 \frac{f_1 f_i^2}{f_1^2 + f_i^2} e^{\frac{pH-8}{0.56}} + 0.52 \left( 1 + \frac{T_{TD}}{43} \right) \left( \frac{S}{35} \right) \frac{f_2 f_i^2}{f_2^2 + f_i^2} e^{-\frac{h}{6}} + 0.00049 f_i^2 e^{-\left( \frac{T_{TD}}{27} + \frac{h}{17} \right)} \quad (9)$$

The first and second terms of Equation (9) represent the relaxation frequencies of two compounds in the ocean: Boric Acid ( $f_1 = 2.2$ ) and Magnesium Sulfate ( $f_2 = 205.3$ ). The third term of the equation represents viscous absorption, in which  $S$  is salinity in ppt,  $h$  is water depth in m, and  $f_i$  is the acoustic frequency applied.

The third term in Equation (6) equals echo strength (in counts) converted to reverberation levels, in which  $K_c$  is a factor for the conversion of amplitude in counts (as reported by the ADCP receiver circuit) to dB.  $E$  is the RSSI (returned signal strength indicator), given by the Aquadopp sensor for each bin along the acoustic beam, in counts [33]. Reference echo strength ( $E_r$ ) was zero, under the assumption of null noise level.

SSC or  $c$  was obtained in mg/L from OBS measurements based on a previous calibration for conditions in the study area following the instructions by the manufacturer [34], where it was obtained the linear relationship between Nephelometric Turbidity Unit, NTU, (as an independent variable) and mg/L (as a dependent variable), as shown by equation 10, with significant correlation coefficients at a 99.5% confidence level (i.e., the average magnitude of the residuals was less than 0.5% of the measurement range).

$$Turbidez(NTU) = 0.473 * c(\text{mg/L}) - 701 \quad (10)$$

In order to estimate SSC values, a calibration curve was obtained, relating ABS (in dB, as estimated from the Aquadopp current meter) to suspended sediment concentration  $c$  (in mg/L, measured with a calibrated OBS 3+) through simple linear regression analysis.

Obtaining the calibration curve involves collecting simultaneous measurements between both variables. Using the best-fit model, the SSC values were estimated in the study area. Finally, the relationship between echo intensity from acoustic measurement from Aquadoop (dB) and SSC values derived from OBS (mg/L) is mathematically represented by:

$$10^{\log(SSC_{OBS})} = a * ABS (in \text{ dB}) + b \tag{11}$$

where  $a$  and  $b$  represent the relationship between both variables. The calibration curve was validated using independent data that was not used in the initial fitting process. The method was implemented for the sensors (W1 to W4, and D1 to D4), and it is explained in more detail in results Section 3.1.

The calibration for the ABS method using an OBS sensor is shown in Appendix A. An important limitation was found in the process for estimating SSC from ADCP, which is associated with the sediment grain size (see Appendix B).

### 2.4.5. Estimation of Suspended Sediment Transport

Flux velocity directions determine sediment transport directions. Onshore-directed or offshore-directed velocities imply cross-shore transport, whereas E-directed or W-directed velocities involve alongshore transport [35]. Sediment flux was calculated as the product of suspended sediment content  $c$  and the respective velocity components ( $u$ -components for cross-shore currents or alongshore currents). In order to calculate values of absolute and relative IG sediment flux, net suspended sediment flux was obtained first for each point, as follows:

$$q_{total} = \langle uc \rangle = \langle (\bar{u} + \tilde{u}) (\bar{c} + \tilde{c}) \rangle = \bar{u} \cdot \bar{c} + \langle \overline{u' \cdot c'} \rangle \tag{12}$$

The first term on the right-hand side of Equation (12) represents the local mean sand flux ( $q_{mean}$ ), and the second term is the oscillatory flux of the wave. The symbol  $\langle \rangle$  indicates that it is a time-averaged value. Oscillatory flux was classified into a wave component (SS) and an IG wave component (IG) using the cutoff frequency,  $f_{split} = 0.05$  Hz.

$$\langle \overline{u' \cdot c'} \rangle = \langle (u_{ss} + u_{IG})(c_{ss} + c_{IG}) \rangle \approx \langle u_{ss} \cdot c_{ss} \rangle + \langle u_{IG} \cdot c_{IG} \rangle \tag{13}$$

Equations (12) and (13) were rewritten as:

$$q_{total} = \langle uc \rangle = \bar{u} \cdot \bar{c} + \langle u_{ss} \cdot c_{ss} \rangle + \langle u_{IG} \cdot c_{IG} \rangle \tag{14}$$

The relative contribution of  $q_{IG}$  to total flux rate was determined as,

$$|q_{IG}| / (|q_{IG}| + |q_{ss}| + |q_{mean}|) \tag{15}$$

The contributions of other components were analogously calculated, and suspended sediment transport was vertically averaged. This allowed us to analyze the effect of SS and IG wave conditions on suspended sediment transport.

## 3. Results

### 3.1. Wave Breaking

The percentage of broken waves was calculated, assessing them from offshore to onshore sensors. This is a critical parameter, useful as a tool for coastal management, but rarely quantified for parametric models of energy dissipation within the inner and outer surf zones. Figure 2a,b show satellite images corresponding to a single measurement day of each climate season. Figure 2c,d show how the percentage of broken waves evolved through time. The percentage of broken waves ranged from 1% to 7%, from the shoaling zone to near the swash zone, for both wet and dry seasons.

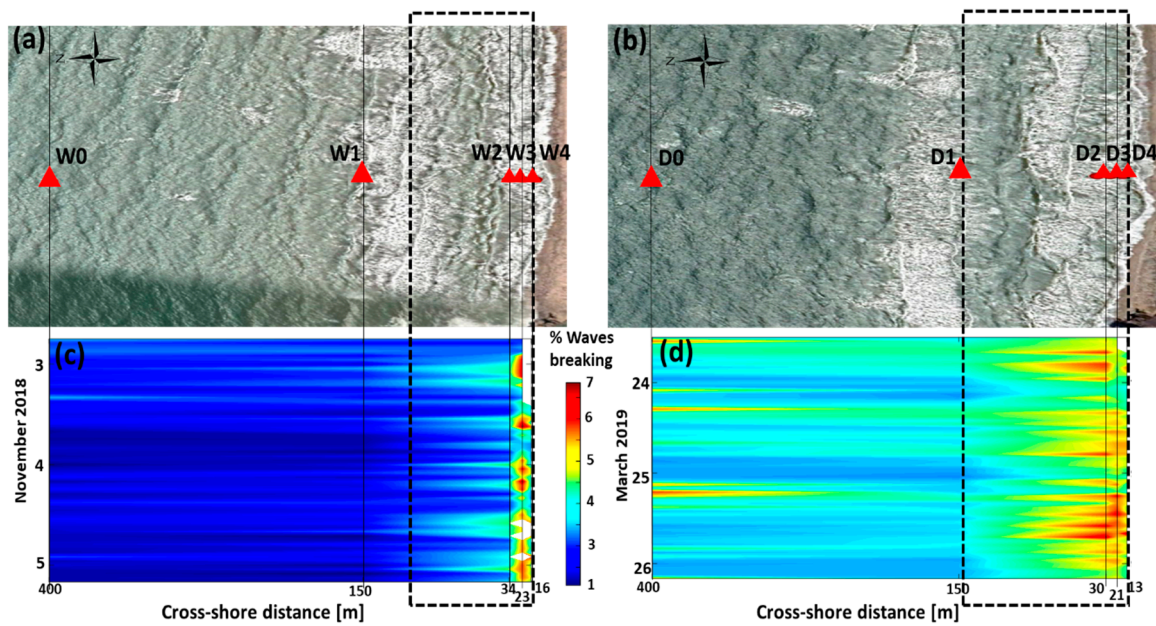


**Figure 2.** (a) Satellite image obtained from Google Earth for the Bocatocino beach for 2018 November (wet season); (b) Satellite image obtained from Google Earth for the Bocatocino beach for 2019 March (dry season). The red triangles correspond to the locations of the pressure and current sensors. (c) Breaking wave’s percentage for the wet season. (d) Breaking wave’s percentage for the dry season. The rectangle represents the zone with a higher breaking wave percentage.

Percentages of broken waves greater than 3.5% (corresponding to the inner surf zone) coincided with the area shown in the dotted rectangle of Figure 2a,b, for both climatic zones. Meanwhile, percentages below 3.5% were identified outside the rectangle (corresponding to the outer surf zone). The width of the breaker zone was related to the climatic season. As shown in Figure 2c,d, the inner surf zone during the dry season was wider in the dry season than during the wet season.

During the dry season, the beach slope was gentler, with a less steep profile (Figure 1e). The resulting surf zone was wide enough to dissipate the energy of most waves. On the other hand, the beach slope was steeper in the wet season (Figure 1e), so the surf zone was narrow, and the incoming energy was reflected with little or no breaking. In addition, it can be inferred from Figure 2c,d that, for the most dissipative intermediate beach (dry season), most wave breaking occurs in the outer border of the breaker zone, intensifying in the middle to inner breaker zone. On the other side, for the intermediate, less dissipative beach (wet season), which had lower energy, most waves break close to the middle surf zone. For more dissipative beaches, this value rapidly increases towards the outer surf zone, whereas for more reflective beaches, the value slowly increases through the entire surf zone. These results agree with conceptual models of the surf zone with gently sloped, dissipative beaches mentioned by [36].

### 3.2. Nearshore Hydrodynamics

Figure 3 represents the spatial-temporal evolution of hydrodynamic forces and SSC during the field experiments. Each variable is calculated by sea states. Figure 3a presents the temporal evolution of sea level for cross-shore sensors located 150 m from the coast. Figure 3b,c show the significant heights of the SS and IG waves ( $H_{mo,SS}$  y  $H_{mo,IG}$ , respectively). Figure 3d,e show cross-shore and long-shore flow velocities, suspended sediment concentration (SSC, Figure 3f), and wave steepness (Figure 3g). The left side represents data taken during the wet season, and the right side comprises data from the dry season.

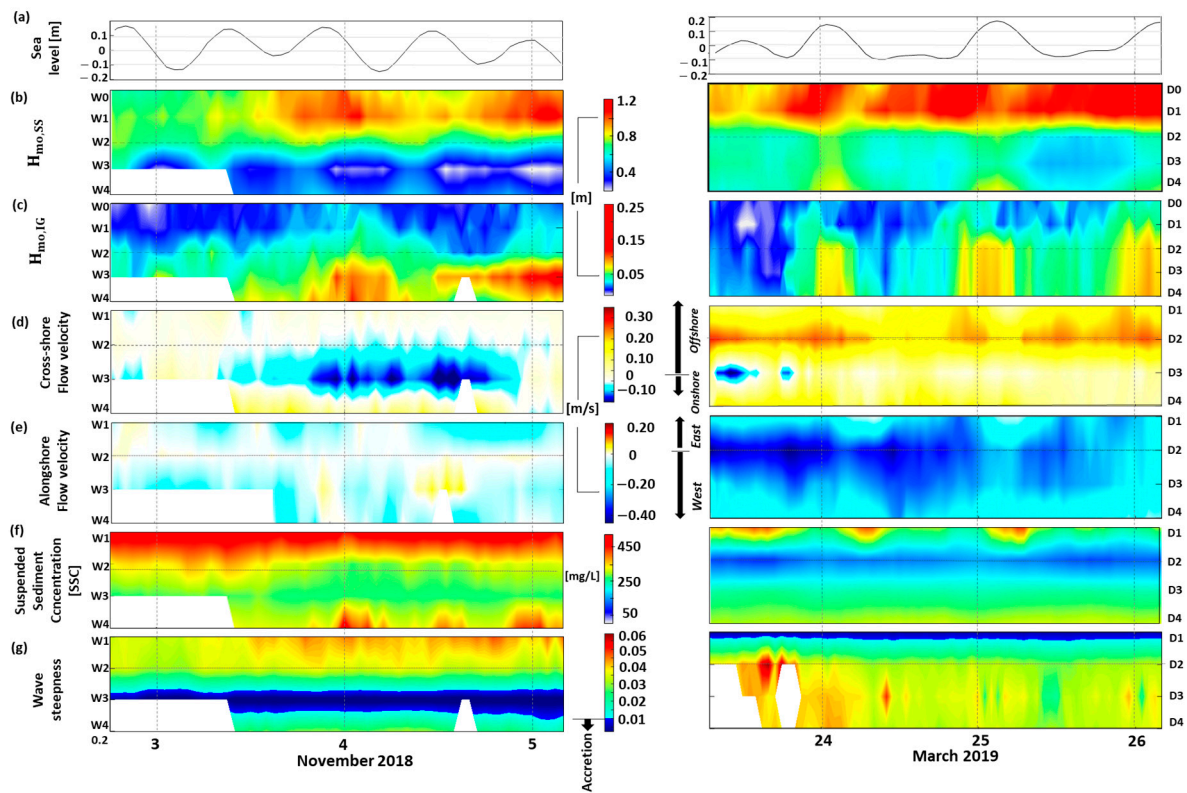


**Figure 3.** (a) Temporal evolution of sea level for cross-shore sensors located at 150 m. Spatial-temporal distribution for: (b) Significant wave height SS ( $H_{mo,SS}$ ). (c) Significant wave height IG ( $H_{mo,IG}$ ). (d) Cross-shore flow velocities. (e) Long-shore flow velocities. (f) Suspended sediment concentration, SSC. (g) Wave steepness. The horizontal line corresponds to 30 m from the coast. In addition, the data were averaged by sea state (hourly) for the wet (left panel) and dry (right panel) seasons.

The definition of shoaling, surf, and swash zones (Table 1) was supported by the results shown in Figures 2 and 3. The shoaling zone was identified in areas with depths greater than 2.8 m, characterized by the absence of broken waves, together with the greatest significant wave height (ss-wave) values on instrument locations W0, W1, D0, and D1. From this point, the waves begin to break, form crests, and significant wave heights increase, whereas ss-waves decrease. In addition, an increase in the percentage of broken waves is recorded. Coarse sands prevailed in this zone (47.7% for the wet season; 36.5% for the dry season, see Table 2). Sensors W4 and D4 were located near the swash zone, where a decrease in the percentage of broken waves was found, suggesting less turbulence and wave breakage activity. In addition, this location was identified to exhibit the lowest energy and height values for SS-waves, but higher values for IG-waves compared with other areas away from the coast. Coarse sediments were distributed near the swash zone during the wet season, with 37.5% of gravel and 34.6% of coarse sand for the dry season. In the dry portion of the beach, ~52% of the middle sand was identified for both climatic seasons.

### 3.2.1. Spatial and Temporal Evolution of SS-Waves and IG-Waves

Figure 3b shows greater height values for SS-waves,  $H_{mo,SS}$ , during the dry season, compared to those in the wet season. In turn, offshore SS-wave height was predominantly greater than onshore SS-wave during the dry season. In Figure 3c, IG-wave  $H_{mo,IG}$ , values were more representative than SS-wave ones within the inner surf zone. This difference was more evident in the dry season (when the beach displayed a more dissipative profile) than during the wet season (when the beach featured a less dissipative profile). This pattern agrees with the works of [37,38], who found that on gently sloping beaches, IG wave heights are relatively greater compared to SS-waves, whereas IG wave heights are

smaller compared to short-wave heights on steep beaches. Differences in wave height may be explained by the morphodynamic state of the Bocatocino beach, which was observed to be less dissipative during the wet season and more dissipative during the dry season. In the same way, it is possible to infer a reflection of  $H_{mo,SS}$  during high tide intervals in the case of the dry season. Relationships between beach profile and wave height patterns at Bocatocino Beach are consistent with the results reported by [39,40]. It is important to point out that the highest atmospheric pressure gradients occurred during the dry season ( $\sim 1010.6$  mbar), in contrast with those of the wet season ( $\sim 1009.3$  mbar) [41]. Differing pressure gradients indicate a significant increase in wind-height fields and SS-wave height during the dry season. On the other hand, during the wet season, the opposite trend was observed (Figure 3b). The meteorological parameters mentioned above were extracted from marine meteorological bulletins published by the General Maritime Directorate (DIMAR) for November 2018 and March 2019 [41].

During the wet season, SS-wave height values were highest in the outer surf zone ( $H_{mo,SS} \approx 0.7$  m to 1.2 m), contrasting with those in the inner surf zone ( $H_{mo,SS} \approx 0.1$  m to 0.6 m). These variations may be caused by energy dissipation and increase due to shoaling. IG-wave height decreased due to friction between the incident short wave group and the seabed. These decreases intensified through two shallow water zones (Figure 2a), inducing breaking points distributed at different depths in the breaking zone, together with the generation of long waves (surges and bores). Therefore, IG-wave height was lower in the inner surf zone ( $H_{mo,IG} \approx 0.05$  to 0.1 m) but increased near the swash zone (up to approximately 0.3 m). These data are in close agreement with the models in [42,43]. In the dry season, SS-wave height was highest in the outer surf zone ( $H_{mo,SS} \approx 0.8$  to 1.2 m), with lower values in the inner surf zone ( $H_{mo,SS} \approx 0.5$  to 0.8 m). These height values decreased due to energy dissipation in wave breaking. IG-wave was relatively lower in the inner surf zone ( $H_{mo,IG} \approx 0.05$ ) but increased near the swash zone (up to approximately 0.08 m).

For both seasons, nearshore SS-wave height values were tide-modulated. In the wet season, the highest SS-wave height values ( $H_{mo,SS} \approx 0.4$  to 0.6 m) were synchronized with the neap-spring tidal cycle, whereas the lowest values of SS-wave height ( $H_{mo,SS} \approx 0.2$  to 0.4 m) coincided with the spring-neap tidal cycle. During the dry season, the highest high tides (lowest low tides), as well as the highest (lowest) SS-wave and IG-wave heights, coincided with maximum ( $H_{mo,SS} \approx 0.8$  m and  $H_{mo,IG} \approx 0.13$  m), and minimum heights ( $H_{mo,SS} \approx 0.4$  m and  $H_{mo,IG} \approx 0.05$  m), respectively. No influence of tides could be identified for IG-wave height.

Energy is dissipated when waves approach shallow waters due to an energy transformation process. SS and IG energy distributions were calculated for cross-shore instruments (400, 150, 34, 23, and 16 m away from the coast) (Figure 4). Figure 4a shows the time series of significant wave height ( $H_s$ ) for marine sensors; Figure 4b,c show the spatial-temporal distribution of SS and IG energies; and Figure 4d shows a time series of sea level. Figure 4b,c show that during the wet season SS energy decreases from the outer surf zone to the inner surf zone, from  $2.99 \text{ m}^2/\text{Hz}$  to  $0.57 \text{ m}^2/\text{Hz}$ , whereas IG energy increases from  $0.05 \text{ m}^2/\text{Hz}$  to  $0.18 \text{ m}^2/\text{Hz}$ . These results indicate that energy is non-linearly transferred from high-frequency (SS) to low-frequency (IG) waves. According to [40,41], this phenomenon occurs mainly on beaches with gentle or intermediate slopes or in high-energy conditions, as observed at Bocatocino Beach. On the other hand, Figure 4b shows that during the dry season, SS energy decreases from the outer surf zone to near the swash zone ( $1.9 \text{ m}^2/\text{Hz}$  to  $0.79 \text{ m}^2/\text{Hz}$ ), whereas IG energy increases from  $0.06 \text{ m}^2/\text{Hz}$  to  $0.18 \text{ m}^2/\text{Hz}$ . These results confirm the relationship between seabed morphology and the percentage of broken waves. This energy transfer may be related to: the generation of leaky waves through the release of group-bound long waves [44]; when bound waves satisfy the free wave dispersion relationship [45,46]; or when time-varying breakpoint forcing occurs [47].

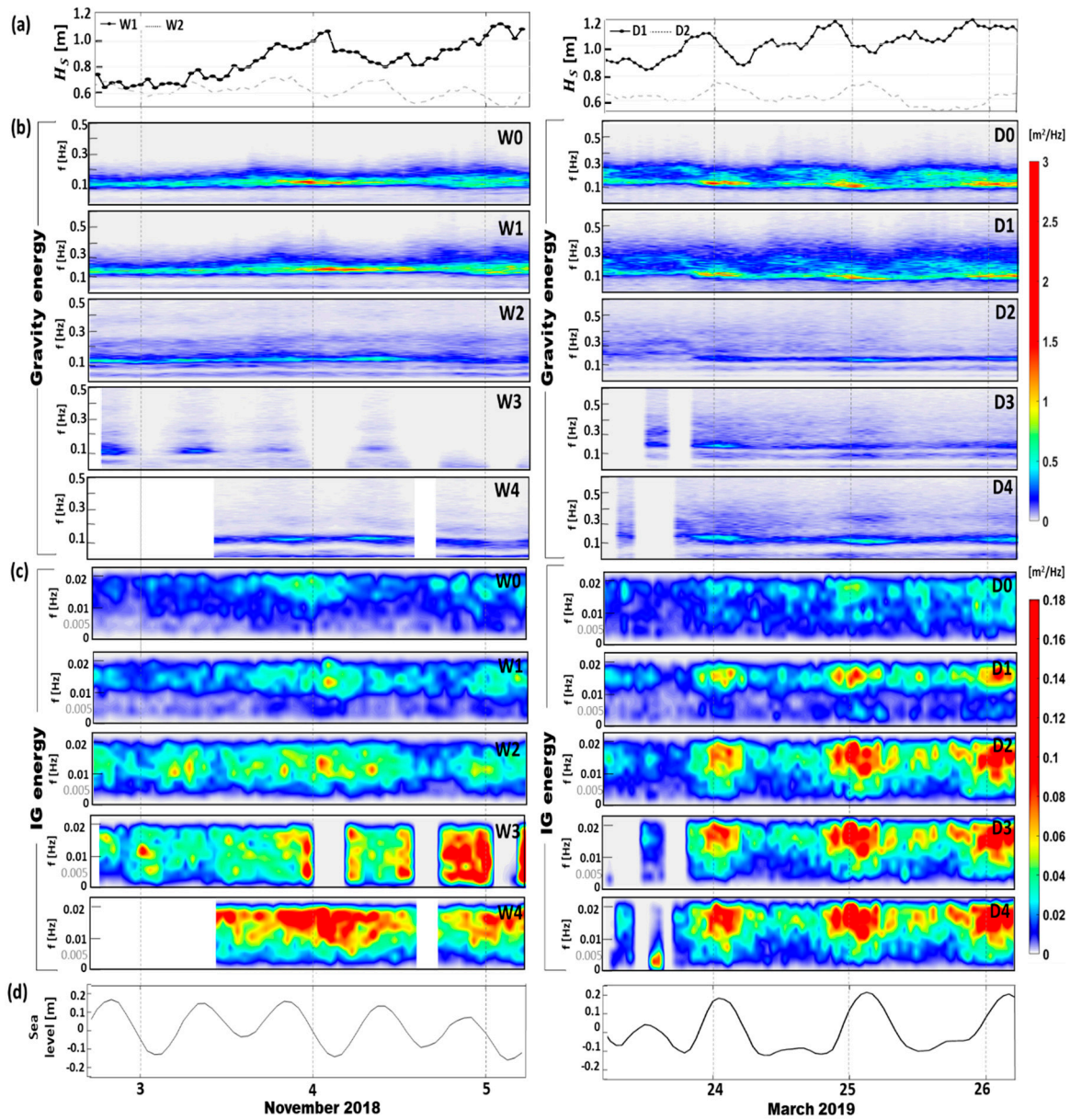


**Figure 4.** SS and IG-energy distribution. (a) Temporal evolution of  $H_s$  for sensors at 150 m (solid black line) and 30 m (dashed gray line) from the coast; (b) Spatial-temporal distribution of IG energy for each sensor located; (c) Spatial-temporal distribution of SS energy for each sensor located, (d) Significant wave height ( $H_s$ ). Data were averaged by sea state (hourly) for the wet (left panel) and dry (right panel) seasons.

Figure 4b,c show the synchronicity between tide cycles and wave regimes for both SS and IG. A decrease in cross-shore SS energy of 81% was observed in the wet season, together with a 58.4% decrease from the outer surf zone to near the swash zone during the dry season. Here, IG waves interact with short waves (particularly around the spectral peak of energy), and energy in the IG frequency propagates to a wide range of high frequencies [37,38]. In contrast, IG energy doubled in both climate stations. IG-waves create higher IG harmonics, shifting IG waves to an asymmetrical shape [38]. According to [48], which points to seabed friction as a possible cause for wave energy dissipation, or who proposes a decrease in energy due to wave breakage [49,50].

### 3.2.2. Spatial and Temporal Evolution of Alongshore and Cross-Shore Currents

Figure 3d,e show the spatio-temporal distribution of cross-shore and long-shore currents for the wet (left-side) and dry (right-side) seasons. In both climatic seasons, cross-shore currents were the dominant type, with a prevailing seaward direction, in contrast with longitudinal currents with a prevailing westward direction. In addition, the greatest intensities for both currents and SS-waves  $H_{mo,SS}$  were observed during the dry season. In both climate seasons, the direction of cross-shore currents was influenced by wave conditions, with currents more oriented towards the coast when IG-wave conditions were more energetic (inner surf zone, Figure 4c). However, current directions became oriented offshore near the swash zone. In the dry season, cross-shore currents displayed particularly strong magnitude and direction and were oriented towards the sea in the shoaling zone when SS-wave conditions were stronger (Figure 4b). On the other hand, there is no prevailing direction of currents during the wet season. This contrast between climatic seasons may be explained by inter-seasonal changes in seabed morphology, which may probably affect current measurements represented by processes in breaking and sandbank formation zones.

Seaward return flows were thus differentiated and identified as undertow currents, possibly generated when SS-waves broke on the different submerged sandbanks observed nearshore. These results are consistent with previous research that corroborates the relationship between wave-breaking processes and the direction of cross-shore currents [51,52]. Current directions depend on nearshore processes where: bank formation processes occur outside the breaking zone (the region where waves rapidly dissipate energy due to depth-limited wave breakage and currents are predominantly directed offshore), and breakage processes occur within the breaking zone and produce currents near the coast.

### 3.3. Inter-Seasonal Changes in Subaerial and Submerged Beach Morphology

Beach profile measurements and nearshore bathymetric datasets allows us to identify erosion and accretion zones on a short-term scale. Bathymetric information was recorded relative to the Mean Low-Water Spring (MLWS), showing seabed geomorphology for each climate season. These data and nearshore hydrodynamics were used to understand the morphological changes of the beach.

#### 3.3.1. The Cross-Shore Suspended Sediment Transport

Figure 5a shows the temporal evolution of significant wave height ( $H_s$ ) for W2, W4, D2, and D4 sensors. Figure 5b,c show the net distribution of cross-shore and alongshore sediment flux, in  $\text{mg}\cdot\text{m}^{-2}\cdot\text{s}^{-1}$ , for SS waves ( $q_{SS}$ ) and IG waves ( $q_{IG}$ ) during the wet and dry seasons, respectively. W2 and D2 sensors were located in the inner surf zone, and W4 and D4 sensors were located near the swash zone.

Sediment fluxes during the dry season were generally found to noticeably exceed the mean total flux. The highest flux peaks were  $q_{SS} = 1.19 \text{ mg}/\text{m}^2\text{s}$  during the wet season and  $q_{IG} = 0.98 \text{ mg}/\text{m}^2\text{s}$  in the dry season. Cross-shore transport was greater than alongshore transport in both climatic seasons, in the same way as corresponding cross-shore currents were greater than alongshore currents. In addition,  $q_{SS}$  was greater than  $q_{IG}$ , both for cross-shore and long-shore transport. Insignificant rates of net suspended sediment transport rates, associated with IG waves, were also found by [8,39]. A particularity stood out during the dry season: fluxes due to SS-waves displayed similar magnitude orders in sensors D3 and D4. However, IG-wave-associated fluxes were significantly greater in sensor D3, where it was found that IG energy and wave breakage processes were more intense (see Figure 5c).

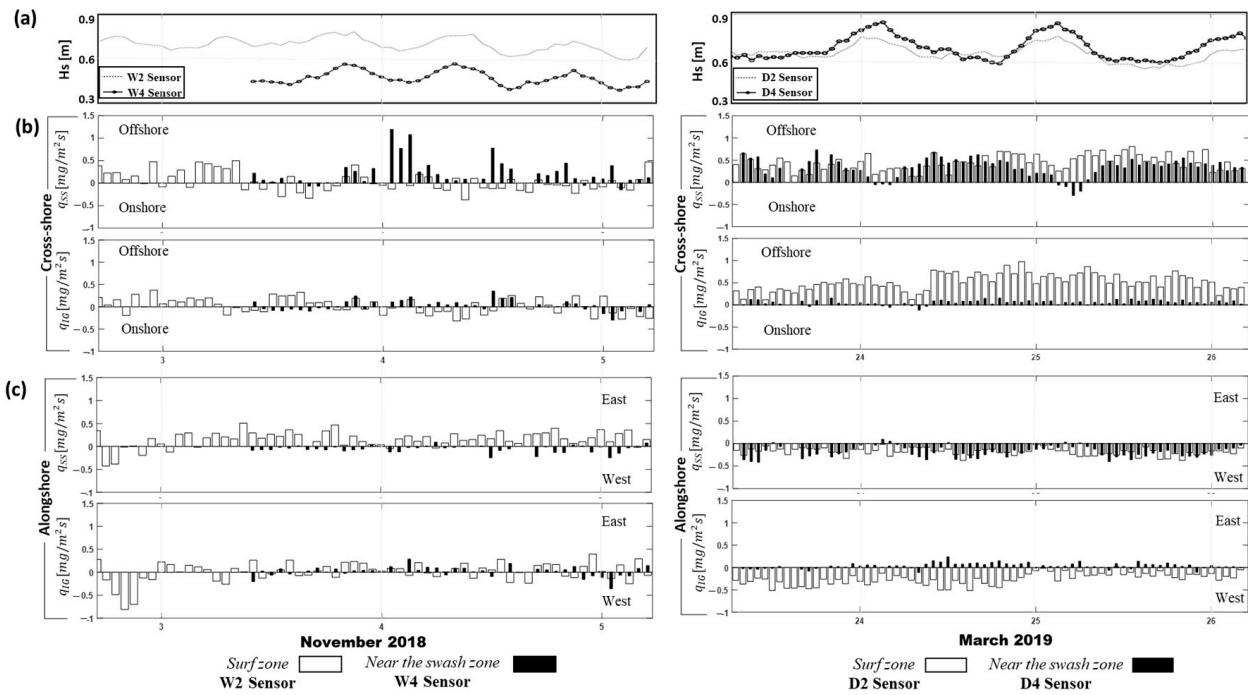


**Figure 5.** Net sediment flux distribution for SS and IG waves ( $q_{SS}$  and  $q_{IG}$ , respectively). (a) Temporal evolution for the significant wave height; (b) Cross-shore sediment flux distribution; and (c) Alongshore sediment flux. The fluxes were calculated for the sensors at 30 m (solid black line in (a) and black rectangle in (b,c)) and 10 m from the coast (dashed gray line in (a) and white rectangle in (b,c)). Data were averaged by sea state (hourly) for the wet (left panel) and dry (right panel) seasons. Since the sediment fluxes were determined by Equation (12) from the measurements of “ $v$ ” and the estimates of “ $c$ ” obtained from the ABS method, both measurements collected from the aquadopp sensors, it follows that the precision of the estimated sediment fluxes is  $\pm 1\%$  of the measured value (accuracy of aquadopp instruments).

During the wet season, cross-shore  $q_{SS}$  displayed maximum and minimum peaks of  $1.19 \text{ mg/m}^2\text{s}$  and  $0.03 \text{ mg/m}^2\text{s}$ , respectively, whereas alongshore  $q_{SS}$  exhibited a maximum value of  $0.51 \text{ mg/m}^2\text{s}$  and a minimum of  $-0.02 \text{ mg/m}^2\text{s}$ . On the other side, cross-shore  $q_{IG}$  showed maximum and minimum peaks between  $0.35 \text{ mg/m}^2\text{s}$  and  $-0.03 \text{ mg/m}^2\text{s}$ , respectively, whereas alongshore  $q_{IG}$  displayed a maximum value of  $-0.81 \text{ mg/m}^2\text{s}$  and a minimum of  $0.03 \text{ mg/m}^2\text{s}$ . In addition, cross-shore  $q_{SS}$  presented a predominantly wave-dominated regime during the dry season, whereas for the wet season, it was not possible to distinguish a prevailing direction. Regarding the flux direction, observed  $q_{SS}$  cross-shore fluxes were mainly offshore-directed (Figure 5b,c, left), whereas  $q_{SS}$  alongshore fluxes in the inner surf zone were directed westward. At the same time, Figure 5c shows that  $q_{SS}$  alongshore fluxes were W-directed near the swash zone. However,  $q_{IG}$  did not show a significant cross-shore direction, particularly in the surf zone. Despite this, these findings may imply that long waves act as suspended sediment advection mechanisms, mainly by breaking incident waves [9]. Wave steepness was greater ( $>0.035$ ) around these sensors, as was average wave height, which reached 0.6 m for sensor W2 and 0.5 m for sensor W4.

In the dry season (Figure 5b,c, right), cross-shore  $q_{SS}$  presented maximum and minimum values of  $0.73 \text{ mg/m}^2\text{s}$  and  $-0.04 \text{ mg/m}^2\text{s}$ , respectively, whereas alongshore  $q_{SS}$  displayed a maximum value of  $-0.34 \text{ mg/m}^2\text{s}$  and a minimum of  $0.03 \text{ mg/m}^2\text{s}$ . On the other hand, cross-shore  $q_{IG}$  presented maximum and minimum values of  $0.98 \text{ mg/m}^2\text{s}$  and  $-0.04 \text{ mg/m}^2\text{s}$ , respectively, whereas alongshore  $q_{SS}$  displayed a maximum value of  $-0.51 \text{ mg/m}^2\text{s}$  and a minimum value of  $0.02 \text{ mg/m}^2\text{s}$ . Regarding the flux direction,  $q_{IG}$  cross-shore flux values were greater than those of  $q_{SS}$  cross-shore flux, the opposite pattern to that found in the wet season. These

were consistent with previous works [53,54], which found that  $q_{IG}$  could exceed sediment transport caused by incoming waves and mean currents. In addition, tidal modulation of IG waves was observed (Figure 5b, right). IG wave height was greater during some tidal cycles (particularly during the neap-spring cycle), so that it drives the highest energy transfer from SS-waves to release IG motions. The values of  $q_{IG}$  alongshore flux were noticeably higher than those of  $q_{SS}$  fluxes (Figure 5c). IG height coming from the surf zone can be almost as important as SS-wave height [7,53]. In summary, cross-shore currents and sediment suspended concentrations resulted in predominantly cross-shore-oriented  $q_{SS}$  and  $q_{IG}$ .

### 3.3.2. The Beach Slope and Morphological Changes of the Subaerial Zone of the Beach

The Bocatocino beach was classified into five sections (Sections S1 to S5, see Figure 1e) for the wet season (blue line) and the dry season (red line). Beach slope and volume changes were calculated, especially in the nearshore zone. In turn, this will allow for the development of a detailed analysis of the main changes in the seabed. Section S1 was located next to the coast, with a very steep slope ( $4.9^\circ$ ) for the wet season and a gentler slope ( $1.7^\circ$ ) for the dry season. Section S2 (between 16 and 62 m from the coast) exhibited a concave profile during the wet season and a slope of  $0.9^\circ$  during the dry season. In section S3 (between 61 and 124 m), there is a gentle slope of approximately  $0.5^\circ$  for the wet season and  $0.6^\circ$  for the dry season. Section S4 (between 124 and 238 m) features a slope of approximately  $1.2^\circ$ , and Section S5 (between 238 and 400 m) exhibits a slope of  $1.0^\circ$  in both climatic seasons. Regarding the changes in beach sediment volume ( $\text{m}^3/\text{m}$ ), a decrease of  $13.3 \text{ m}^3/\text{m}$  of sediment was identified in Section S1. In Section S2, sediment volume increased by  $25.5 \text{ m}^3/\text{m}$ , and decreased by  $13.4 \text{ m}^3/\text{m}$  in Section S3. Volume increased to  $689 \text{ m}^3/\text{m}$  in Section S4. Lastly, the sediment volume in Section S5 did not show any variations.

Volume changes may be related to seasonal variations in hydrodynamic forces (waves and currents). Additionally, an offshore sensor (Aquadopp profiler, 400 kHz, located at 600 m from the coast) was employed to understand inter-seasonal changes at a 3-h measurement rate, from 1 November 2018 to 24 March 2019. Figure 6 shows offshore hydrodynamic conditions ( $H_{sOffshore}$  and  $T_{pOffshore}$ ). The highest peak values were identified using circles with  $H_{sOffshore}$  values between 1.7 and 2.3 m and  $T_{pOffshore}$  ranging from 8 to 10.8 s. These values occurred in January, February, and March, in agreement with those reported by [55] for the Colombian Caribbean. These results indicate that hydrodynamic forces occur more frequently during these months, due to the wave energy conditions (mainly due to ENE winds). Maximum values of  $H_{sOffshore}$  and  $T_{pOffshore}$  occurred in 23 January and 12 March 2019, which can be associated with two cold fronts affecting the Caribbean region of Colombia, including Bocatocino Beach, according to marine meteorological bulletins issued by DIMAR and its Center for Oceanographic and Hydrographic Research of the Caribbean [50]. These events come from the Northwestern Caribbean Sea between the Yucatan Peninsula and Cuba, moving towards the Southeast and generating abundant clouds and moderate precipitations. However, these cold fronts became stationary fronts, weakening until they disappeared.

The aforementioned intense events could explain the significant volume changes between climate seasons, as these meteorological events tend to remain for prolonged periods of time. Therefore, these events may have a more significant long-term influence on microtidal beach morphology on the Colombian Caribbean coast compared to other energetic wave states [16,17]. However, there is no compelling evidence supporting a direct relationship between volume changes and hydrodynamic conditions for the interval January–March (Figure 6).

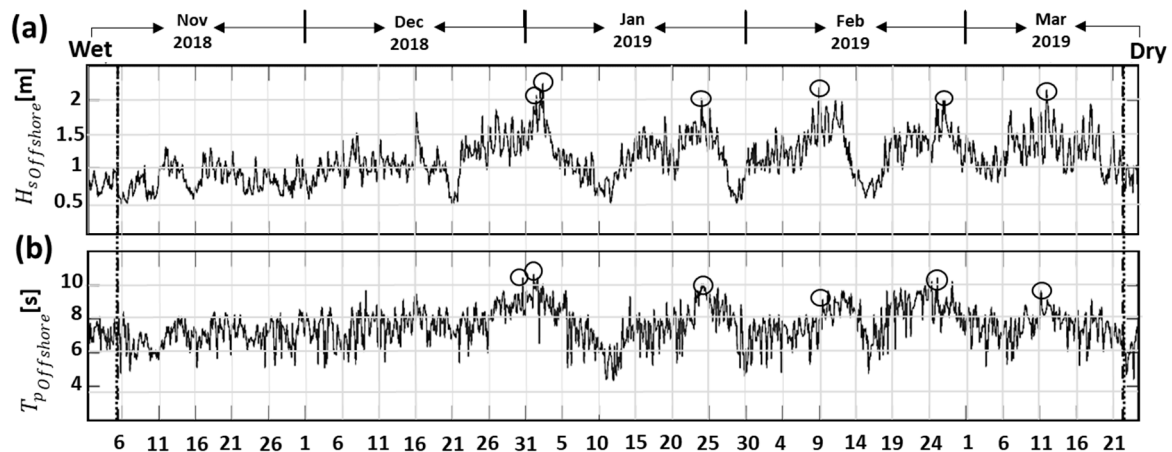


**Figure 6.** Temporal evolution of the offshore conditions from the  $S_{offshore}$  sensor located at 600 m from the coast with measurements from 1 November 2018 to 24 March 2019. (a) Significant wave height ( $H_{sOffshore}$ ). (b) Peak period: ( $T_{pOffshore}$ ). The circles indicate the most energetic waves recorded during the measurement period. In addition, the dotted vertical lines divide the measurement days of each campaign (1 to 3 November 2018 and 22 to 25 March 2019).

Figure 1c,d show no evidence of abrupt morphological change in the offshore sections (S4 and S5) between climate seasons. However, these changes were identified at the inner surf zone (sections S2 and S1), where IG-wave energy was higher and is considerably dynamic due to different turbulence processes that may occur in this zone [10,56]. Lastly, these findings are very representative, allowing us to approach an understanding of morphological seabed changes, considering the complexity of measurements at the inner surf zone [7].

### 3.3.3. The Wave Steepness as a Control Parameter in the Formation and Migration of Submerged Bar

In order to assess the natural supply of sediment to the beach, SSC estimates were compared to wave steepness (Figure 3f,g), and the relationship between them was observed. Wave steepness was used as a control parameter to understand hydrodynamic processes and their relationship with estimated SSC values on the coast, as well as with coastal currents. Accretion and erosion zones for both seasons were determined based on the conceptual model for suspended sediment transport and intertidal beach morphology response [57]. In the wet season and near the swash zone, cross-shore currents were offshore-directed when SSC values were greatest (approximately 450 mg/L), and wave steepness ranged between 0.04 and 0.05. As the wave propagates from the surf zone and gets near the swash zone, currents become onshore-directed where the slope is less than 0.01. The obtained results indicate an accretion zone 30 m away from the coast (blue band on the left side of Figure 3g). The accretion zone may be explained by a greater SSC (400 mg/L) close to the outer surf zone and sediments that were transported onshore-directed and deposited at the inner surf zone. These findings highlight the weak undertow observed nearshore when bathymetric gradients were generally smaller.

During the dry season, cross-shore currents were offshore-directed in the shoaling zone, while the wave steepness value was less than 0.01. These results indicate the presence of an accretion zone 150 m from the coast (blue band on the right side in Figure 3g) with average SSC values of 350 mg/L. For its part, the lowest SSC values (~150 to 250 mg/L) were found in the inner surf zone. The strong undertow observed nearshore may have contributed to sediment transport towards the sea. Therefore, it is possible to infer that sediment was not locally deposited but rather supplied from outside the study area. In short, the nearshore behavior trend for the beach was predominantly accretionary when

SS-waves were weaker, that is, with wave slopes below 0.010. On the other hand, the beach was prone to erosion when SS-waves were stronger, with wave slope values above 0.010.

The sediments during the wet season were identified as being coarser than those in the dry season near the swash zone. So, in W2, the greatest values of wave height and energy were recorded for the wet season, and a submerged bar was identified. Given the previous conditions, the bar could be acting as a natural filter, trapping coarser particles and allowing finer sediment to be deposited in other areas. This dynamic may be influenced by high IG energies in the wet season, facilitating transport and favoring the deposition of coarser particles compared to the dry season. The ss-wave energy was greater in the offshore direction, which could lead to the transport of larger particles directed toward deeper waters, explaining the appearance of coarser sands in this zone, whereas middle sands, being less coarse, may be transported by waves up to the subaerial beach.

### 3.3.4. Inter-Seasonal Volume Variability and the Emerged Beach Morphology

Figure 7a shows four cross-shore topographic profiles (P1, P2, P3, and P4), measured from the top of the dry beach (~1.5 m MLWS) to the low tide line. Profiles P1-P2 and P3-P4 were located on each side of the hydrodynamic sensor array. The longest profile was 33 m. Figure 7b shows daily values of dry beach volume, estimated from topographic profiles (1 and 4 November 2018; 24 and 25 March 2019).

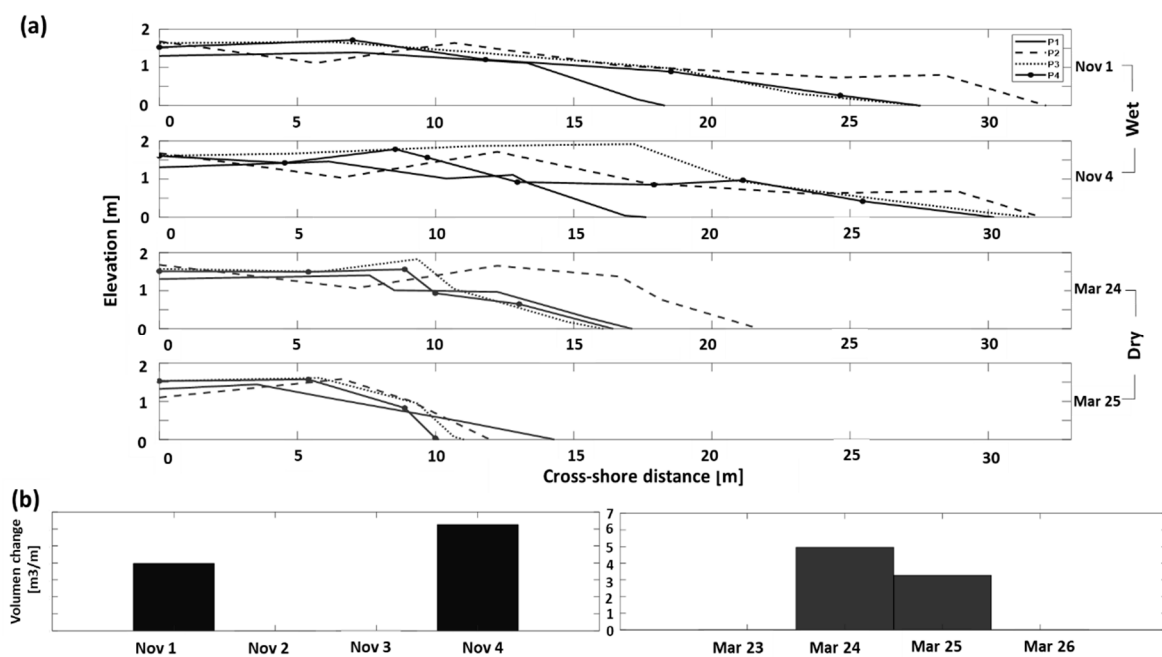


**Figure 7.** Topography profiles and daily volume changes for the Bocatocino Beach, (a) Topographic profiles measured for the wet and dry seasons. (b) Daily volumetric changes of the dry beach for the wet season (left side) and dry season (right side).

On November 1 and 4, 2018, the highest part of the dry beach (~1.5 m M.L.W.S) was relatively flat in all profiles, but around 12 m slopes differed from each other. On November 1, the maximum slope of P1, located at approximately 14 m, was  $13.5^\circ$ , whereas P2 featured a slope of  $9.9^\circ$  at approximately 28 m. P3 and P4 displayed a similar morphology, with a maximum slope of  $8.4^\circ$  at 19 m. On November 4, P1 showed a slope of  $13.5^\circ$  at approximately 17 m. Profile P4 featured a slope of  $11^\circ$  at 9 m, then an almost flat slope up to 21 m, followed by a gentle slope of  $6.2^\circ$ . In general terms, no significant differences were observed between profiles P1 and P2, whereas P3 and P4 showed a wider coastal stripe in which geofoms (such as bars and/or berms) are present on the highest part of the dry beach. This may be explained by the increase in long-shore currents, predominantly

directed towards the east, which would transport sediment from P2 to profiles P3 and P4. Figure 8b shows an increase in beach volume of  $2.3 \text{ m}^3/\text{m}$  (accretion) between November 1 and 4. This increase is potentially associated with sediment interchange among suspended particles near the coast (Figure 3f) and the accretion zone located near W3 (Figure 3g).

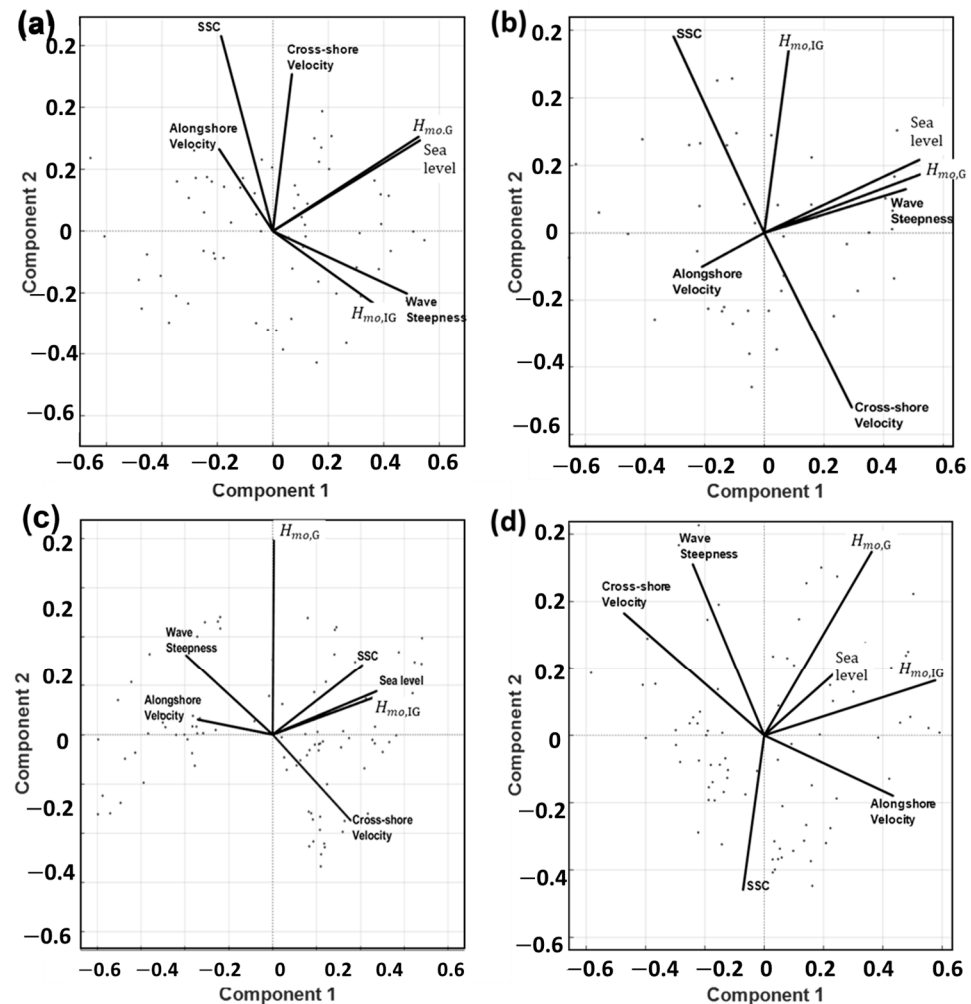


**Figure 8.** PCA biplot between SSC and hydrodynamic forcing factors:  $H_{mo,G}$ ,  $H_{mo,IG}$ , cross-shore and alongshore currents, wave steepness, sea level, for wet season: (a) inner surf zone, (b) near the swash zone, and for dry season: (c) inner surf zone, and (d) near the swash zone.

On 24 and 25 March 2019, all four profiles maintained a similar topography, almost flat up to 5 m. The subaerial beach did not show significant morphological changes, as cross-shore hydrodynamic forces remained constant in this measurement period (Figure 3c,d). On 24 March, profiles P1, P3, and P4 exhibited a similar topography, with two pronounced slopes, one of  $29.5^\circ$  at 9 m, and a maximum slope of  $14.4^\circ$  at 12 m. P2 showed a maximum slope of  $10.7^\circ$  at 18 m. On 25 March, P3 and P4 exhibited a maximum slope of  $14.7^\circ$  at 9 and 8.5 m, respectively. Figure 8b shows a decrease of  $1.7 \text{ m}^3/\text{m}$  (erosion) between 24 and 25 March. In Bocatocino Beach, bars were steeper on 24 March, flattening and migrating towards the coast on 25 March. The results herein described are consistent with submerged bar movement and cross-shore current directions, both predominantly oriented onshore during the wet season. Therefore, sediment availability will be greater in the dry portion of the beach. On the other hand, during the dry season, submerged bar movement and cross-shore currents were offshore-directed, resulting in less sediment availability in the dry portion of the beach.

In addition, the dry season stood out for the presence of two cold fronts in the Caribbean Sea, incoming from the Yucatan Peninsula, which caused changes in wind speed and direction affecting the Western Caribbean Sea, as reported by the CIOH [41]. It was established that the combination of meteorological and marine energy conditions during the transition from two climatic seasons affected the beach morphology.

3.4. Physical Factors Controlling Suspended Sediment Transport Using PCA

A PCA (principal component analysis) was applied to investigate the hydrodynamic-morphological interactions in a microtidal intermediate-dissipative beach under low to moderate wave energy conditions. The PCA results were illustrated in a two-dimensional biplot graph. In this graph, the axes (principal components) are linear combinations of the original variables, explaining most of the variability [58]. Variables with different contributions to a given principal component tend to occupy opposing areas in the plane. Figure 8 shows the first two principal components of the PCA between SSC and hydrodynamic variables such as SS-wave height, IG-wave height ( $H_{mo,SS}$ ,  $H_{mo,IG}$ ), cross-shore currents, alongshore currents, sea level, and wave steepness. PCA correlation coefficients are listed in Table 3. In this study, correlations above 0.45 were deemed relevant. The first principal component accounts for 11–12% of the variance between the surf and swash zones and 15–16% near the swash zone. The second principal component accounts for 11–14% of the variance between the surf zone and near the swash zone and 12–14% near the swash zone.

**Table 3.** Correlations between  $H_{mo,G}$ ,  $H_{mo,IG}$ , cross-shore and alongshore currents, wave steepness, sea level, and SSC-estimated for both climatic seasons at two coastal zones (first: inner surf zone, and second: near the swash zone). The higher correlations were from 0.45.

Season/Coastal Zone	Wet/Inner Surf Zone		Wet/Near the Swash Zone		Dry/Inner Surf Zone		Dry/Near the Swash Zone	
	1st Principal Component	2nd Principal Component						
$H_{mo,G}$	0.52	0.3	0.52	0.17	0.01	0.79	0.36	0.55
$H_{mo,IG}$	0.36	−0.23	0.08	0.54	0.47	0.15	0.58	0.16
Sea level	0.53	0.29	0.52	0.22	0.48	0.18	0.25	0.19
Wave steepness	0.49	−0.2	0.49	0.13	−0.4	0.32	−0.24	0.51
Cross-shore currents	0.07	0.51	0.29	−0.52	0.36	−0.35	−0.5	0.36
Alongshore currents	−0.19	0.27	−0.21	−0.1	−0.34	0.06	0.43	−0.17
SSC	−0.19	0.63	−0.3	0.57	0.41	0.28	−0.07	−0.48
Variance	11%	11%	12%	14%	15%	12%	16%	14%

Figure 8a shows the results of the PCA during the wet season, which indicate a close relationship between cross-shore currents ( $r = 0.51$ ) and SSC ( $r = 0.63$ ), between the surf zone and near the swash zone. Therefore, when cross-shore currents are more intense, the supply of suspended sediments will be highest, but SSC will be lower when cross-shore currents are weaker. The first component showed a positive correlation between  $H_{mo,SS}$  ( $r = 0.52$ ), and sea level ( $r = 0.53$ ), and gravity energy modulation due to tides. On the other hand, Figure 8b shows a negative correlation between cross-shore currents ( $r = -0.52$ ) and SSC ( $r = 0.57$ ) near the swash zone. This can be explained because cross-shore currents were offshore-directed near the swash zone. Therefore, less suspended sediment will be available towards the coast (Figure 3d,f). In addition, relevant positive correlations with  $H_{mo,IG}$  ( $r = 0.54$ ) and SSC ( $r = 0.57$ ) were found, allowing us to infer that a high  $H_{mo,IG}$  could increase SSC or vice versa. This indicates that SSC was predominantly wave-influenced (see Figure 3c,f). SSC was not correlated with other hydrodynamic forcing factors ( $H_{mo,SS}$ , sea level, wave steepness, and alongshore currents).

Figure 8c represents the results of the PCA for the dry season. The first component indicates a weak correlation between  $H_{mo,IG}$  ( $r = 0.47$ ) and sea level ( $r = 0.48$ ) between the surf zone and near the swash zone. However, there was no higher correlation between SSC and hydrodynamic forces. The first principal component indicated a strong negative correlation between cross-shore currents ( $r = -0.50$ ) and  $H_{mo,IG}$  ( $r = 0.58$ ) near the swash zone. This can be corroborated by the observation of currents being stronger near the swash zone when  $H_{mo,IG}$  values were lowest, and vice versa (Figure 3c,d). At the same time, Figure 8d shows a less negative correlation between  $H_{mo,SS}$  ( $r = 0.55$ ) and SSC ( $r = -0.48$ ) in the second principal component. The first and second principal components confirmed a strong correlation between  $H_{mo,SS}$ , and wave steepness.

PCA results show that, during the wet season, SSC and cross-shore currents are strongly correlated to the second principal component. For the dry season, a less positive correlation was found between cross-shore currents ( $r = 0.36$ ) and SSC ( $r = 0.41$ ) within the surf and wash zones, as well as a less negative correlation between cross-shore currents ( $r = 0.36$ ) and SSC ( $r = -0.48$ ) near the swash zone. Therefore, a low correlation between alongshore currents and SSC can be confirmed for the studied beach.

#### 4. Discussion

Hydrodynamic variables (SS- and IG-waves, cross-shore and alongshore currents, and wave steepness), together with patterns of sediment dynamics (cross-shore and alongshore sediment transport, formation and migration of submerged bars, identification of erosion and accretion zones, and nearshore volume changes), are further discussed to analyze the relationships between hydrodynamic forces and beach morphology during dry and wet seasons.

##### 4.1. Implications of Indirect SSC Estimates for Suspended Sediment Transport

Despite the estimation method used (OBS or ABS), the SSC time series followed identical trends (Figure A1e). Even though there are some differences between measured and estimated sediment concentrations, these results are acceptable and indicate that the use of ABS is a reliable method for estimates of SSC and, therefore, for the estimation of net suspended sediment transport. It must be taken into account that quantifying net sediment transport remains a difficult task, given that reliable and precise measurements of sediment transport rates are essential for understanding the morphological changes of the beach. Several factors may explain the slight differences found between both SSC estimation methods. Acoustic sensors are generally sensitive to particle characteristics, such as size and shape [59]. For example, these sensors are unable to detect particles smaller than the wavelength of the acoustic pulse, which in turn depends on the type of instrument employed. Previous works indicate that optic sensors are more sensitive to clay particles [60], whereas acoustic instruments are more sensitive to sand. In this study, overestimates were found to be related to the acoustic sensor, in agreement with [61], who found that acoustic sensors might overestimate sediment concentrations on sandy beaches under turbulence conditions. It is worth mentioning that, in this work, measurements were taken between the surf and near the swash zone in the context of textural properties typical of a gravelly sand beach.

Despite the conditions under which field measurements were carried out (covering the breakage zone with constant, high turbulence levels), which may affect sensor data [62], together with the time and cost involved, the results of this work indicated a good level of correlation. Different improvements have been developed for the ABS method. An additional calibration was applied for this problem [63], yielding an SSC estimate that remained unaltered within turbulent, small-scale eddies (following the Kolmogorov scale). A review and update of the equations and concepts presented by [33] was made by [28], in order to provide information necessary for its use in newer devices. Even though the ABS method was originally applied only to estuary, bay, and river settings [29,30,63], it has also been used in studies of coastal zones, such as high-turbulence beaches. For example, it

employed the ABS method and obtained a reasonably good correlation between acoustic and optic backscattering estimates of SSC for a reflective beach in storm and non-storm conditions [5].

#### 4.2. The Role of Cross-Shore Currents in Suspended Sediment Transport

The PCA revealed that cross-shore currents prevailed over alongshore currents, as was the case for sediment transport, in both climatic seasons. In addition, it was found that SSC and cross-shore current values were highest nearshore. So, this is a predominantly cross-shore-dominated system due to beach orientation (WE/EW, i.e., parallel to the coastline) playing an important role in sediment transport, probably where incident waves that arrived perpendicularly to the coast, without oblique incidence, most of the time. In these conditions, the wavefront is parallel to the beach, resulting in currents and sediment transport that are predominantly cross-shore-oriented. Similar results were discussed by [64], who showed that sediment transport has an important role as a driver of beach evolution processes such as shoreline shifts and bar migration. This study found a particular behavior in the wet season relative to changes in the direction of cross-shore currents, depending on wave conditions. This behavior is consistent with the observed direction of cross-shore sediment transport (Figure 6b). When values of offshore wave height and peak period ( $H_{sOffshore}$  and  $T_{pOffshore}$ ) were at their lowest, sediment transport was also at its lowest level, as observed on 3 and 4 November 2018. This cross-shore sediment transport may be causing the sediment interchange observed between the accretion zone identified near the swash zone (Figure 3e) and the emerged portion of the beach (Figure 8b).

Sediment flux did not show a prevailing direction during the wet season. This contrasts with the greater, predominantly offshore flux observed in the dry season, caused by the strong intensity of cross-shore currents. Therefore, the accretion zone observed 150 m away from the coast (Figure 3g, right) may result from cross-shore sediment transport towards the sea in the surf zone (Figure 3d, right). At the same time, erosion in the dry beach area (Figure 8, right) may be due to strong cross-shore currents directed towards the sea, near the swash zone. These findings highlight the possible role of undertow currents in transporting sediment from the dry beach area to the sea. The results are consistent with [65], who attributed offshore sediment flux to undertow (undercurrent) extending beyond the breakage zone. This work is also consistent with previous research reporting stronger undertow currents on steep beaches than on gentle ones [66]. However, sediment transport at Bocatocino Beach was predominantly offshore, with higher intensity during the dry season, when the beach profile was mostly dissipative. The results of this research indicate that onshore and offshore sand migration (Figure 3g) was caused by cross-shore transport, together with nearshore sediments in suspension due to the combined action of tides, winds, waves, and currents. In general terms, this research allowed us to observe how suspended sediment transport responded and interacted with (1) high-frequency waves, (2) low-frequency waves, and (3) undertow currents.

#### 4.3. Contribution of SS and IG Wave Energy to Suspended Sediment Transport

Even though waves are not the main mechanism of sediment transport on the study beach, the results of this work reveal their important role in seabed morphology. An energy transfer from high to low frequencies was observed when waves were moving onshore and were disturbed by the seabed until they broke (Figures 3b and 5c). In this regard, Ref. [13] found that, in the subaerial beach, cross-shore sediment transport is mediated by the equilibrium between the effect of oscillatory wave movement and that of middle currents. This research assessed the role of oscillatory flux (due to SS-wave and IG-wave) and its effect on morphological changes experienced by Bocatocino Beach.

SS-wave energy was greater in the outer surf zone than near the swash zone. However, SS-waves showed the opposite behavior in both climate seasons. In a similar way, during the dry season, cross-shore  $q_G$  was significantly higher in the inner surf zone, decreasing near the swash zone. These observations are consistent with previous works [39,67], which

indicate that SS-waves might be the most important component of sediment transport in the surf zone and near the swash zone, where the percentage of broken waves was higher. Cross-shore  $q_{IG}$  was higher in the surf zone (with a lower break wave percentage) than near the swash zone (with a higher percentage). These findings agree with previous works [68,69], reporting that IG-wave transport is lower with moderate waves than under high energy conditions. Nearshore IG-waves found in this work lie within the Leaky Infragravity Wave category. In some cases, this type of wave may increase undertow currents in the surf zone [70,71]. In this study, the greatest undertow intensities occurred in the dry season, when a smaller extent of beach area was present. However, it is not possible to infer that Leaky IG Waves caused the erosion observed on the beach during the transition between one climate season and the next. This interpretation cannot be totally discarded, however, due to the reported antecedents, particularly in a well-differentiated erosion zone (Figure 8, right) on Bocatocino Beach.

The presence of an accretion zone (Figure 8, left) may be due to a greater availability of sediment near the swash zone during the wet season, with outstanding onshore current intensities. On its part, the results indicate the dependence of SSC on wave energy, allowing us to infer that SS-waves are typically acting as agents of sediment agitation, whereas currents play a role in transport. Regarding transport and wave energy, the results of this work are consistent with previous research in coastal zones with non-breaking wave conditions (lower-energy waves). These studies found that transport processes are generally directed landward, a pattern that results in accretion processes on the beach. On the other hand, during high energy conditions with a high percentage of broken waves (e.g., storm cycles), the beach and coastal dune zone are strongly affected by incoming waves, usually resulting in erosion processes [72].

#### 4.4. Relationship between Wave Steepness and Beach Morphological Changes

The relationship between wave height and wavelength, better known as wave steepness, has been traditionally recognized as a factor influencing beach morphology [73,74], a relationship that has been confirmed by later works [4,75]. Wave steepness could thus be used to determine submerged bar migration nearshore and beach morphological changes occurring between climatic seasons. In this way, the interaction between nearshore accumulated sediment (represented by the accretion zone ~23 m from the coast) and sediment flux direction (cross-shore and onshore) might be the result of significant accumulation (Figure 8b) during the wet season. However, during the dry season, the accretion zone shifted to a position approximately 150 m away from the coast, with a predominantly offshore flux direction and low availability of suspended sediment nearshore. These conditions may have led to the creation of a zone of high erosion (Figure 8, right). The aforementioned patterns show that onshore sediment transport was often observed when wave steepness was less, whereas sediment was transported offshore in high wave steepness conditions [4]. This relationship was further verified through PCA results, which highlighted the relationship between wave steepness and significant wave height. The PCA shows that, for both climate seasons, wave steepness increases with wave height. This finding emphasizes the importance of wave inclination as a parameter to distinguish erosion and accretion zones on a beach [58,76,77]. A limit between erosion and accretion of 0.01 was employed by [77] on a fine gravel beach at Slapton Sands (United Kingdom). On the other hand, [57] considered wave inclination values below 0.01 as indicative of normal behavior with accretion and above 0.01 as an indicator of erosive behavior in a macrotidal beach at Mariakerke, Belgium. In summary, even though wave steepness is an acceptable proxy for the identification of wave asymmetry and the direction of fluid movement [78], previous research recommends exercising caution when using this criterion for sandy beaches [79].

#### 4.5. Interactions between Suspended Sediment Transport and Morphological Changes on the Nearshore Subaerial Beach

Cross-shore sediment transport is considered a driving factor in beach topographical change [13,80]. This was verified by this work, as cross-shore sediment transport was significantly greater than alongshore transport between the surf zone and near the swash zone. Morphological changes were described in terms of daily variations in beach volume for each climate season. In the wet season, sediment transport was predominantly onshore when wave conditions were gentle (maximum  $H_{m0} = 1$  m and maximum  $T_p = 8.6$  s). In contrast, during the dry season, sediment was transported onshore when wave conditions were strong (maximum  $H_{m0} = 1.2$  m and maximum  $T_p = 8.6$  s). These results indicate a seasonal pattern, with beach volumes greater during the wet season and smaller during the dry season. Other authors have also related erosive events to strong wave conditions and accretion events to moderate wave conditions [81]. Likewise, sediment transport on the submerged beach was analyzed through migrating bars, revealing that submerged bars moved onshore in moderate wave conditions. Sandbank migration under strong wave conditions has been proposed by previous studies [82]. The sediment transport reported in this study (forcing erosion and accretion in the dry part of the beach), together with the migration of submerged bars, are consistent with previous assessments of the relationship between morphodynamic cycles and wave energy conditions in microtidal and mesotidal sand beaches [81,83,84].

Regarding sediment textural features, finer sediments moved offshore in the surf zone, whereas coarser sediments were found in the surf zone and near the swash zone. The same pattern was observed by [85], who found an onshore transport trend for coarser sediments, whereas finer sediments moved offshore.

### 5. Conclusions

The relationship between hydrodynamic forcing, suspended sediment transport, and the intermediate-dissipative microtidal beach morphology was analyzed using in situ measurements during the dry and wet seasons. Hydrodynamic drivers (waves, tides, and currents) were characterized, and the response of topographical profiles to these drivers was analyzed both for the submerged and emerged beaches. The results show that cross-shore currents are the prevailing hydrodynamic forces in nearshore sediment transport. These currents forced the migration of a submerged bar during the transition between the wet and dry seasons. The accumulation of the submerged bar intensified during the wet season when the wave height intensities were lower, contrary to what was observed during the dry season.

The ABS method for indirect estimation of suspended sediment transport for the microtidal intermediate-dissipative beach allowed for reasonably good results, considering that measurements were carried out between the surf zone and near the swash zone. However, caution must be exercised when using optical or acoustic equipment to estimate sediment concentrations. Such measurements may lead to significant overestimates or underestimates of sediment transport, due to instrument sensitivity to different grain sizes. It should not be left aside that acoustic measurements may be affected by turbulence. Nevertheless, correcting these parameters should significantly improve these measurements, particularly those obtained with acoustic backscattering.

On the subaerial beach of the dry beach, daily changes in sediment supply were strongly correlated to wave energy and current directions nearshore. SS-waves and cross-shore currents contributed mainly by transporting suspended sediments. During the dry season, strong cross-shore currents were identified, and erosion zones were differentiated. On the other hand, a greater amount of deposited sediment was evident when IG-wave heights, SS-wave heights, and cross-shore currents were lower. High IG wave energy (intensified from the inner surf zone) may cause sediment agitation in this zone, which is accentuated during the wet season.

Wave conditions during the dry season were very strong, leading to a more pronounced response in beach morphology. However, morphology variations in a microtidal intermediate-dissipative beach depend not only on wave conditions but also on currents and SSC. Therefore, currents, SSC, and waves are driving factors of nearshore sediment supply influencing daily topographical change. As a result, Bocatocino Beach, which is wave-dominated, exhibits daily accretion and erosion states. Wave inclination was an important indicator of beach evolution, particularly regarding the formation and migration of submerged bars.

The results of this study explain the microtidal intermediate-dissipative beach morphology. It was found that there was a significant accretion nearshore on the subaerial beach during the wet season when there was a greater availability of sediments, the SS-wave heights nearshore were lower, and sediment flux was directed onshore. In the dry season, the opposite behavior was observed, and a notorious erosion was distinguished. The results represent a significant contribution to understanding the morphological behavior of the beach and its relationship with hydrodynamic forces. Therefore, it must be taken into account that, unlike laboratory tests under controlled conditions, there is no control over the environmental variables present in the study area. According to the results of this study, it is recommended to use numerical modeling to estimate beach evolution and coastal transport in the middle and long term (months to years). This study establishes a baseline for future coastal geomorphology research, contributing to the understanding of the hydrodynamic-morphological interactions in a microtidal intermediate-dissipative beach under low to moderate wave energy conditions.

**Author Contributions:** Conceptualization, A.M.G.; Methodology, A.M.G., L.O., S.O. and J.C.; Software, A.M.G.; Validation, A.M.G.; Formal analysis, A.M.G.; Investigation, A.M.G.; Writing—original draft, A.M.G.; Writing—review & editing, A.M.G. and L.O. All authors have read and agreed to the published version of the manuscript.

**Funding:** The authors thank the Ministerio de Ciencia Tecnología e Innovación for the financial support.

**Institutional Review Board Statement:** Not applicable.

**Informed Consent Statement:** Not applicable.

**Data Availability Statement:** The data presented in this study are available on request from the corresponding author.

**Acknowledgments:** The authors thank the Coastal Engineering and Processes Laboratory of Sisal Academic Unit—UNAM for its facilities and support. The authors thank Alec Torres Freyermuth of the Coastal Engineering and Processes Laboratory, Universidad Nacional Autónoma de México (UNAM), Puerto de Abrigo s/n, Sisal, Yucatán.

**Conflicts of Interest:** The authors declare no conflict of interest.

## Appendix A

The ADCP analysis for SSC estimates requires calibration data obtained through direct SSC measurements. Both the D2 current meter and the OBS turbidity sensor were used for this purpose, as both instruments were captured in a time-synchronized manner. Figure A1 illustrates the methods employed to deduce sediment concentration from acoustic echo intensity data obtained with the D2 current meter. Figure A1a shows the D2 sensor depth-time series, together with the tide cycle (6 h) for which the ABS method calibration was made. The time series of acoustic echo intensity for sensor D2 (in counts) versus SSC estimates from the OBS (in mg/L) are shown in Figure A1b. Figure A1c represents the SSC empiric model derived from OBS and acoustic echo intensity from sensor D2. Figure A1d is a scatter plot between OBS-derived and D2-derived SSC for a tide cycle at a rate of 60 s. The relationship between suspended sediment concentrations (SSC) obtained with the D2 sensor (mg/L) and direct sampling using OBS (mg/L) from 23 to 25 March 2019, averaged at a rate of 1 h, is shown in Figure A1f.

Equation (5) was split into three steps. In the first term, reference values of  $L_{DBM} = 2.23$ ,  $C = -129.5$ , and  $P_{DBW} = 12.6$  were used following [33]. To establish the second term, the range along the beam was obtained from ADCP Nortek,  $R = 0.52$  m (in agreement with the manufacturer’s instructions). To define the acoustic absorption coefficient  $\alpha$ , reference values of  $S = 35$  ppt,  $h = 2.1$  m,  $T_{TD} = 29.5$  °C, and  $f = 2$  MHz were used. Regarding the relaxing frequencies of two main compounds in seawater, values of  $f_1 = 2.4$  and  $f_2 = 238$  were determined for Boric acid and Magnesium Sulfate, respectively.

In order to establish the third term, a scaling factor  $K_c$  of 0.42 counts/dB was calculated using the Equation (7) and a  $T_{TD} = 29.5$  °C. This value is consistent with the  $K_c$  ranges between 0.40 and 0.47, which were reported by [86,87]. This value was determined taking into account that all current meter systems are from the same manufacturer (Nortek), therefore using the same family of components for measuring echo amplitude [88]. The relationship between echo intensity from ABS (dB) and SSC derived from OBS (mg/L) was obtained from simple linear regression analysis (Figure A1c):

$$SSC_{OBS} = 10^{1.227 * ABS \text{ (in dB)} - 441.8} \tag{A1}$$

It is worth highlighting that internal count units can be linearly transformed to dB in a range of 70 dB with an approximate precision of 1–2 dB [30]. In this study, backscattering values from the three beams were averaged, as the exact orientation of Aquadopp relative to the OBS sensor is unknown.

The sensor D2 underestimated most OBS values (Figure A1e). The model obtained for SSC calibration was significant at  $R^2 =$  of 0.69, with a Willmott coefficient of 0.75, and an RMSE of 8.5. These results could be attributed to the characteristics of suspended sediment particles, such as size, shape, and color, which may affect measurements taken with the acoustic sensor [59,60]. However, the results are a satisfactory proxy for SSC when not enough turbidity instruments are available in the field, particularly considering that acoustic sensors may be sensitive to turbulence [63]. When using this model with oceanographic parameters of  $T_{TD} = 29.5$  °C and  $S = 35$ , the values of SSC in the study area ranged from 90 to 150 mg/L, distributed from the surface to the seabed.

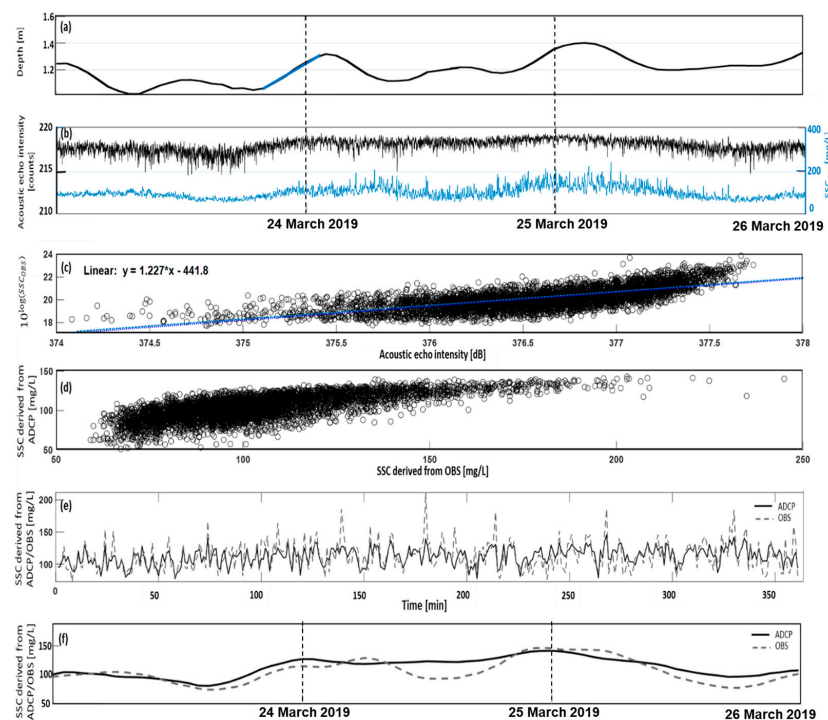


**Figure A1.** ABS method for converting acoustic intensity from ADCP (D2 sensor) to SSC. (a) Depth-time series measured for the D2 sensor; the tidal cycle (flow) used for the calibration of the ABS method was

plotted as a blue line over the complete time series. (b) Echo intensity-time series for the acoustic echo intensity of the D2 sensor, in counts (black line and left y-axis) and SSC derived from OBS, in mg/L (blue line and right y-axis) at a rate of 1 s, (c) Simple linear regression analysis for OBS-derived SSC and acoustic echo intensity from ADCP. (d) Scatter plot between OBS-derived and D2-derived SSC. (e) Time series of OBS-derived SSC (dotted line) and D2 sensor-derived SSC (solid line) for a tidal cycle (blue line in (a)) at a rate of 1 min. (f) Time series of the 1-h average between the OBS-derived SSC (dashed line) and D2 sensor-derived SSC (solid line) from 23 to 26 March 2019. The methodology was calibrated using the OBS and D2 sensors, considering that both sensors were connected to synchronize data. Note: The Aquadopp Profiler (D2) is a highly versatile Acoustic Doppler Current Profiler.

### Appendix B

Taking that into account, the optical sensor exhibited higher sensitivity for small-size particles [19]. Thus, here the concentration volume conversion (in  $\mu\text{L}/\text{L}$ ) to SSC (in  $\text{mg}/\text{L}$ ) was implemented using the LISST-200X sensor and the equation by [51]:

$$SSC \left( \frac{\text{mg}}{\text{L}} \right) = VC \left( \frac{\mu\text{L}}{\text{L}} \right) * \rho_{\text{sediment}} \left( \frac{\text{kg}}{\text{L}} \right) * \frac{1 \text{ L}}{10^6 \mu\text{L}} * \frac{10^6 \text{ mg}}{1 \text{ kg}} * \left( 1 - \frac{\rho_{\text{sediment}} - \rho_{\text{flocule}}}{\rho_{\text{sediment}} - \rho_{\text{water}}} \right) \quad (\text{A2})$$

Equation (A2),  $\rho_{\text{sediment}}$  was established from the average sediment density of 2.63 Kg/L taken from the granulometric analysis of sediment samples collected, while  $\rho_{\text{flocule}}$  was established as 1.15 Kg/L according to [89]. VC was taken from the measured data of the LISST-200X sensor. Once the SSC values (in  $\text{mg}/\text{L}$ ) were obtained, the ABS method was implemented using the D4 sensor, an Aquadopp Profiler HR, which will allow a corroborating effect of particle size D50 on the estimation of SSC through the ABS method (Figure A2). The LISST-200X sensor allowed estimating the SSC classifying by grain size from 1 to 500  $\mu\text{m}$ .

In Figure A2, it was found that particles below 465.6  $\mu\text{m}$  (i.e., middle, fine, and very fine sands, as well as middle, fine, and very fine silts) have the highest scattering values among SSC deduced from D4 data (in  $\text{mg}/\text{L}$ ) and SSC deduced from LISST-200X data ( $\text{mg}/\text{L}$ ), with a Pearson correlation coefficient of up to 71.5% and an R2 of 0.89. This contrasts with the largest particles, which show a Pearson coefficient below 53.2%. It demonstrates an important limitation for estimating SSC from ADCP, which is associated with the grain size of the sample. So, the underestimates registered in Figure A1d may thus be attributed to the presence of larger particles. In this way, the sensitivity of the acoustic sensor to grain size was verified.

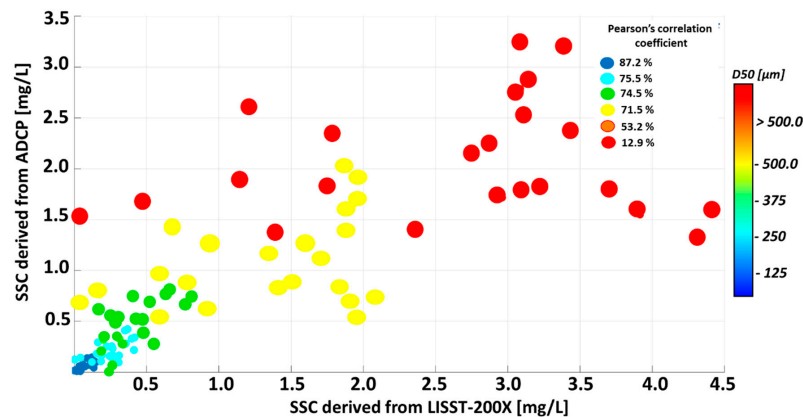


**Figure A2.** Effect of particle size D50 on the estimation of SSC through the ABS method using a LISST-200X sensor near the swash zone in the dry season. Note: The D4' sensor is an Aquadopp Profiler (a highly versatile Acoustic Doppler Current Profiler, ADCP).

A greater sensitivity of acoustic sensors to sand particles was found by [90], which supports the findings. An effect of particle size on SSC estimates was also described by [61,87], who recognized the relationship between particle size and acoustic frequency as a major limitation for the ABS method of SSC estimation.

## References

- Biausque, M.; Senechal, N. Seasonal morphological response of an open sandy beach to winter wave conditions: The example of Biscarrosse beach, SW France. *Geomorphology* **2019**, *332*, 157–169. [CrossRef]
- Bagnold, R.A. Sand movement by waves: Some small-scale experiments with sand of very low density. *J. Inst. Civ. Eng.* **1947**, *27*, 447–469. [CrossRef]
- Wright, L.D.; Thom, B.G. Coastal depositional landforms: A morphodynamic approach. *Prog. Phys. Geogr.* **1977**, *1*, 412–459. [CrossRef]
- Brand, E.; Montreuil, A.; Houthuys, R.; Chen, M. Relating Hydrodynamic Forcing and Topographic Response for Tide-Dominated Sandy Beaches. *J. Mar. Sci. Eng.* **2020**, *3*, 151. [CrossRef]
- Aagaard, T.; Hughes, M.; Baldock, T.; Greenwood, B.; Kroon, A.; Power, H. Sediment transport processes and morphodynamics on a reflective beach under storm and non-storm conditions. *Mar. Geol.* **2012**, *326*, 154–165. [CrossRef]
- Trowbridge, J.; Elgar, S. Turbulence Measurements in the Surf Zone. *J. Phys. Oceanogr.* **2001**, *31*, 2403–2417. [CrossRef]
- Ruessink, B.G. Observations of turbulence within a natural surf zone. *J. Phys. Oceanogr.* **2010**, *40*, 2696–2712. [CrossRef]
- Conley, D.C.; Beach, R.A. Cross-shore sediment transport partitioning in the nearshore during a storm event. *J. Geophys. Res.* **2003**, *108*, C06011. [CrossRef]
- Aagaard, T.; Greenwood, B. Oscillatory infragravity wave contribution to surf zone sediment transport—the role of advection. *Mar. Geol.* **2008**, *251*, 1–14. [CrossRef]
- Aagaard, T.; Hughes, M. Breaker turbulence and sediment suspension in the surf zone. *Mar. Geol.* **2010**, *271*, 250–259. [CrossRef]
- Vidal, C.; Losada, M.A.; Medina, R.; Losada, Í. Modelos de Morfodinámica de Playas. *Ing. Del Agua* **1995**, *2*, 55–74. [CrossRef]
- IOC. 2022. Available online: <https://iocaribe.ioc-unesco.org/en/member-countries/colombia> (accessed on 15 May 2022).
- Aagaard, T.; Greenwood, B.; Hughes, M. Sediment transport on dissipative, intermediate and reflective beaches. *Earth Sci. Rev.* **2013**, *124*, 32–50. [CrossRef]
- Restrepo, J.; Otero, L.; Casas, A.; Henao, A.; Gutiérrez, J. Shoreline changes between 1954 and 2007 in the marine protected area of the Rosario Island Archipelago (Caribbean of Colombia). *Ocean Coast. Manag.* **2012**, *69*, 133–142. [CrossRef]
- Pérez, R.; Ortiz, R.; Bejarano, A.; Otero, D.; Restrepo, L.; Franco, A. Sea breeze in the Colombian Caribbean coast. *Atmosfera* **2018**, *31*, 389–406. [CrossRef]
- Otero, L.; Ortiz-Royero, J.; Ruiz-Merchán, J.; Higgins, A.; Henriquez, S. Storms or cold fronts: What is really responsible for the extreme waves regime in the Colombian Caribbean coastal region? *Nat. Hazards Earth Syst. Sci.* **2016**, *16*, 391–401. [CrossRef]
- Cueto, J.; Otero, L. Morphodynamic response to extreme wave events of microtidal dissipative and reflective beaches. *Appl. Ocean Res.* **2020**, *101*, 102283. [CrossRef]
- Poveda, G. La hidroclimatología de Colombia: Una síntesis desde la escala inter-decadal hasta la escala diurna por ciencias de la tierra. *Rev. Acad. Colomb. Cienc.* **2004**, *107*, 201–222.
- Conde-Frias, M.; Otero, L.; Restrepo, J.; Ortiz, J.; Ruiz, J.; Osorio, A. Experimental analysis of infragravity waves in two eroded microtidal beaches. *Acta Oceanol. Sin.* **2017**, *36*, 31–43.
- Anfuso, G.; Rangel-Buitrago, N.; Correa Arango, I.D. Evolution of Sandspits along the Caribbean Coast of Colombia: Natural and Human Influences. In *Sand and Gravel Spits. Coastal Research Library*; Randazzo, G., Jackson, D., Cooper, J., Eds.; Springer: Cham, Switzerland, 2015.
- IDEAM, TIEMPO Y CLIMA. Available online: [http://www.ideam.gov.co/web/tiempo-y-clima/cartilla-pronostico-pleamares-bajamares-costa-atlantica-colombiana?p\\_p\\_id=110\\_INSTANCE\\_sgxGOQ77WWFo&p\\_p\\_lifecycle=0&p\\_p\\_state=normal&p\\_p\\_mode=view&p\\_p\\_col\\_id=column-1&p\\_p\\_col\\_count=1](http://www.ideam.gov.co/web/tiempo-y-clima/cartilla-pronostico-pleamares-bajamares-costa-atlantica-colombiana?p_p_id=110_INSTANCE_sgxGOQ77WWFo&p_p_lifecycle=0&p_p_state=normal&p_p_mode=view&p_p_col_id=column-1&p_p_col_count=1) (accessed on 6 June 2022).
- Blott, S.; Pye, K. GRADISTAT: A grain size distribution and statistics package for the analysis of unconsolidated sediments. *Earth Surf. Process. Landf.* **2001**, *26*, 1237–1248. [CrossRef]
- Holthuijsen, L. *Waves in Oceanic and Coastal Waters*; Cambridge University Press: Cambridge, UK, 2007.
- Roelvink, J.A.; Stive, M.J.F. Bar generating cross-shore flow mechanisms on a beach. *J. Geophys. Res.* **1989**, *94*, 4785–4800. [CrossRef]
- Masselink, G.; Hughes, M.G.; Knight, J. *Introduction to Coastal Processes and Geomorphology*, 2nd ed.; Hodder Education: London, UK, 2011.
- Battjes, J.A.; Janssen, J.P.F.M. Energy loss and set-up due to breaking of random waves. *Coast. Eng.* **1978**, *1978*, 569–587.
- Fabbri, S.; Giambastiani, M.S.; Sisti, F.; Scarelli, F.; Gabbianelli, G. Geomorphological analysis and classification of foredune ridges based on Terrestrial Laser Scanning (TLS) technology. *Geomorphology* **2017**, *295*, 436–451. [CrossRef]
- Mullison, J. Backscatter estimation using broadband acoustic Doppler current profilers—Updated. In Proceedings of the ASCE Hydraulic Measurements & Experimental Methods Conference, Durham, NH, USA, 9–12 July 2017; pp. 9–12.

29. Lohrmann, A. Monitoring Sediment Concentration with Acoustic Backscattering Instruments. Technical Report 03, Nortek AS. Available online: <https://www.nortekgroup.com/assets/documents/Monitoring-sediment-concentration-with-acoustic-backscattering-instruments.pdf> (accessed on 20 June 2022).
30. Gartner, J.W. Estimating suspended solids concentrations from backscatter intensity measured by acoustic Doppler current profiler in San Francisco Bay, California. *Mar. Geol.* **2004**, *211*, 169–187. [[CrossRef](#)]
31. Vandebroek, E.; Claeys, S.; Plancke, Y.; Verwaest, T.; Mostaert, F. *Agenda for the Future—Hydrodynamics and Sediment Dynamics in the Schelde Estuary: Sub Report 11—Factual Data Report for Frame-Measurements at Drempele van Frederik in December 2015 and January 2016; Version 3.0*. FHR Reports, 14\_024\_11; Flanders Hydraulics Research & Antea Group: Antwerp, Belgium, 2017.
32. Ainslie, M.A.; McColm, J.G. A simplified formula for viscous and chemical absorption in seawater. *J. Acoust. Soc. Am.* **1998**, *103*, 1671–1672. [[CrossRef](#)]
33. Deines, K.L. Backscatter Estimation Using Broadband Acoustic Doppler Current Profilers. In Proceedings of the IEEE Sixth Working Conference on Current Measurement, San Diego, CA, USA, 13 March 1999.
34. Campbell Scientific (CANADA) Corp. OBS-3A Turbidity and Temperature Monitoring System. Operator’s Manual. Available online: [https://s.campbellsci.com/documents/ca/manuals/obs-3a\\_man.pdf](https://s.campbellsci.com/documents/ca/manuals/obs-3a_man.pdf) (accessed on 20 February 2019).
35. De Bakker, A.T.M.; Brinkkemper, J.A.; van der Steen, F.; Tissier, M.F.S.; Ruessink, B.G. Cross-shore sand transport by infragravity waves as a function of beach steepness. *J. Geophys. Res.* **2016**, *121*, 1786–1799. [[CrossRef](#)]
36. Svendsen, I.A.; Madsen, P.A.; Hansen, J.B. Wave characteristics in the surf zone. *Coast. Eng.* **1978**, *520*–539. [[CrossRef](#)]
37. Ruju, A.; Lara, J.; Losada, I. Radiation stress and low-frequency energy balance within the surf zone: A numerical approach. *Coast. Eng.* **2012**, *68*, 44–55. [[CrossRef](#)]
38. De Bakker, A.; Herbers, T.; Smit, P.; Tissier, M.; Ruessink, B.G. Nonlinear infragravity-wave interactions on a gently sloping laboratory beach. *J. Phys. Oceanogr.* **2015**, *45*, 589–605. [[CrossRef](#)]
39. Ruessink, B.G.; Houwman, K.T.; Hoekstra, P. The systematic contribution of transporting mechanisms to the cross-shore sediment transport in water depths of 3 to 9 m. *Mar. Geol.* **1998**, *152*, 295–324. [[CrossRef](#)]
40. Guza, R.T.; Thornton, E.B. Ascend/descend oscillations on a natural beach. *J. Geophys. Res.* **1982**, *87*, 483–491. [[CrossRef](#)]
41. DIMAR, 2020. Cecoldo. Repositorio Digital Marítimo, Fluvial and Costero. Available online: <https://cecoldodigital.dimar.mil.co/view/divisions/ISSN/> (accessed on 5 November 2022).
42. Janssen, T.T.; Battjes, J.A. Long waves induced by short-wave groups over a sloping bottom. *J. Geophys. Res.* **2003**, *108*, 3252. [[CrossRef](#)]
43. Battjes, J.A.; Bakkenes, H.J.; Janssen, T.T.; van Dongeren, A.R. Shoaling of subharmonic gravity waves. *J. Geophys. Res.* **2004**, *109*, C02009. [[CrossRef](#)]
44. Masselink, G. Group bound long waves as a source of infragravity energy in the surf zone. *Cont. Shelf Res.* **1995**, *15*, 1525–1547. [[CrossRef](#)]
45. Baldock, T.E. Dissipation of incident forced long waves in the surf zone—Implications for the concept of “bound” wave release at short wave breaking. *Coast. Eng.* **2012**, *60*, 276–285. [[CrossRef](#)]
46. Contardo, S.; Symonds, G. Infragravity response to variable wave forcing in the nearshore. *J. Geophys. Res. Ocean.* **2013**, *118*, 7095–7106. [[CrossRef](#)]
47. Symonds, G.; Huntley, D.A.; Bowen, A.J. Two-dimensional surf beat: Long wave generation by a time-varying breakpoint. *J. Geophys. Res.* **1982**, *87*, 492. [[CrossRef](#)]
48. Pomeroy, A.; Lowe, R.; Symonds, G.; Van Dongeren, A.; Moore, C. The dynamics of infragravity wave transformation over a fringing reef. *J. Geophys. Res.* **2012**, *117*, C11022. [[CrossRef](#)]
49. Van Dongeren, A.; Battjes, J.; Janssen, T.; van Noorloos, J.; Steenhauer, K.; Steenbergen, G.; Reniers, A. Shoaling and shoreline dissipation of low-frequency waves. *J. Geophys. Res.* **2007**, *112*, C02011. [[CrossRef](#)]
50. De Bakker, A.T.M.; Tissier, M.F.S.; Ruessink, B.G. Shoreline dissipation of infragravity waves. *Cont. Shelf Res.* **2014**, *72*, 73–82. [[CrossRef](#)]
51. Komar, P. *Beach Processes and Sedimentation*, 2nd ed.; Prentice-Hall: Englewood-Cliffs, NJ, USA, 1998.
52. Elgar, S.; Raubenheimer, B.; Guza, R.T. Current Meter Performance in the Surf Zone\*. *J. Atmos. Ocean. Technol.* **2001**, *18*, 1735–1746. [[CrossRef](#)]
53. Beach, R.A.; Sternberg, R.W. Infragravity driven suspended sediment transport in the swash, inner and outer surf zone. In Proceedings of the Specialty Conference on Quantitative Approaches to Coastal Sediment, Seattle, WA, USA, 25–27 June 1991; pp. 114–128.
54. Russell, P.E. Mechanisms for beach erosion during storms. *Cont. Shelf Res.* **1993**, *13*, 1243–1265. [[CrossRef](#)]
55. Ortiz, J.; Otero, L.; Restrepo, J.; Ruiz, J.; Cadena, M. Cold fronts in the Colombian Caribbean Sea and their relationship to extreme wave events. *Nat. Hazards Earth Syst. Sci.* **2013**, *11*, 2797–2804. [[CrossRef](#)]
56. Battjes, J.A. Surf-Zone Dynamics. *Annual Review of Fluid Mechanics. Ann. Rev. Fluid Mech.* **1988**, *20*, 257–293. [[CrossRef](#)]
57. Brand, E.; Montreuil, A.; Dan, S.; Chen, M. Macro-tidal beach morphology in relation to nearshore wave conditions and suspended sediment concentrations at Mariakerke, Belgium. *Reg. Stud. Mar. Sci.* **2018**, *24*, 97–106. [[CrossRef](#)]
58. Bocard, D.; Gillet, F.; Legendre, P. *Numerical Ecology with R Use R*; Springer Science + Business Media: New York, NY, USA, 2011; pp. 115–140.

59. Brand, E.; Montreuil, A.-L.; Chen, M. The effect of turbulence and particle size on suspended sediment concentration measurements in the intertidal zone. In *Coastal Sediments*; Tampa: St. Pete, FL, USA, 2019.
60. Battisto, G.M.; Friedrichs, C.T.; Miller, H.C.; Resio, D.T. Response of OBS to Mixed Grain Size Suspensions during Sandy Duck'97. In Proceedings of the 4th International Symposium on Coasting Engineering and Science of Coastal Sediment Processes, Hauppauge, NY, USA, 21–23 June 1999; Volume 99, pp. 297–312.
61. Brand, E.; Chen, M.; Montreuil, A.L. Optimizing measurements of sediment transport in the intertidal zone. *Earth-Sci. Rev.* **2020**, *200*, 103029. [[CrossRef](#)]
62. Merckelbach, L.; Ridderinkhof, H. Estimating suspended sediment concentration using backscatter from an acoustic Doppler profiling current meter at a site with strong tidal currents. *Ocean Dyn.* **2006**, *56*, 153–168. [[CrossRef](#)]
63. Nauw, J.J.; Merckelbach, L.M.; Ridderinkhof, H.; van Aken, H.M. Long-term ferrybased observations of the suspended sediment fluxes through the Marsdiep inlet using acoustic Doppler current profilers. *J. Sea Res.* **2014**, *87*, 17–29. [[CrossRef](#)]
64. Ding, Y.; Styles, R.; Kim, S.; Permenter, R.; Frey, A. Cross-Shore Sediment Transport for Modeling Long-Term Shoreline Evolution. *J. Waterw. Port Coast. Ocean. Eng.* **2020**, *147*, 4. [[CrossRef](#)]
65. Masselink, G.; Black, K.P. Magnitude and cross-shore distribution of bed return flow measured on natural beaches. *Coast. Eng.* **1995**, *25*, 165–190. [[CrossRef](#)]
66. Aagaard, T.; Black, K.P.; Greenwood, B. Cross-shore sediment transport in the surf zone: A field-based parameterization. *Mar. Geol.* **2002**, *185*, 283–302. [[CrossRef](#)]
67. Masselink, G.; Austin, M.J.; O'Hare, T.J.; Russell, P.E. Geometry and dynamics of wave ripples in the nearshore zone of a coarse sandy beach. *J. Geophys. Res.* **2007**, *112*, C10022. [[CrossRef](#)]
68. Aagaard, T.; Greenwood, B. Suspended sediment transport and the role of Infragravity waves in a barred surf zone. *Mar. Geol.* **1994**, *118*, 2348. [[CrossRef](#)]
69. Black, K.; Vincent, C. High-resolution field measurements and numerical modelling of intra-wave sediment suspension on plane beds under shoaling waves. *Coast. Eng.* **2001**, *42*, 173–197. [[CrossRef](#)]
70. Van Rijn, L.C. Prediction of dune erosion due to storms. *Coast. Eng.* **2009**, *56*, 441–457. [[CrossRef](#)]
71. Choi, J.; Roh, M.; Hwang, H. Observing the laboratory interaction of undertow and nonlinear wave motion over barred and nonbarred beaches to determine beach profile evolution in the surf zone. *J. Coast. Res.* **2018**, *34*, 1449–1459.
72. Van Rijn, L.C. *Principles of Sedimentation and Erosion Engineering in Rivers, Estuaries and Coastal Seas*; Aqua Publications: Amsterdam, The Netherlands, 2012; Available online: [www.aquapublications.nl](http://www.aquapublications.nl) (accessed on 20 February 2019).
73. Meyer, R.D. *A Model Study of Wave Action on Beaches*; Department of Civil Engineering, University of California: Berkeley, CA, USA, 1936.
74. Saville, T. Model studies of sand transport along an infinitely straight beach. *Am. Geophys. Union Trans.* **1950**, *31*, 555–556.
75. Masselink, G.; Russell, P.; Turner, I.; Blenkinsopp, C. Net sediment transport and morphological change in the swash zone of a high-energy sandy beach from swash event to tidal cycle time scales. *Mar. Geology.* **2009**, *267*, 18–35. [[CrossRef](#)]
76. Johnson, J.W. Scale effects in hydraulic models involving wave motion. *Trans Amer. Geophys. Union* **1949**, *30*, 517–525.
77. Masselink, G.; Russell, P.; Blenkinsopp, C.; Turner, I. Swash zone sediment transport, step dynamics and morphological response on a gravel beach. *Mar. Geol.* **2010**, *274*, 50–68. [[CrossRef](#)]
78. Larson, M.; Kraus, N.C. *Sbeach: Numerical Model for Simulating Storm-Induced Beach Change*; U.S. Army Engineer Waterways Experiment Station: Vicksburg, MS, USA, 1989.
79. Jackson, N.L. Evaluation of criteria for predicting erosion and accretion on an estuarine sand beach, Delaware Bay, New Jersey. *Estuaries* **1999**, *22*, 215–223. [[CrossRef](#)]
80. Dall, H.J.; Merrifield, M.A.; Bevis, M. Steep beach morphology changes due to energetic wave forcing. *Mar. Geol.* **2000**, *162*, 443–458. [[CrossRef](#)]
81. Ruggiero, P.; Walstra, D.J.R.; Gelfenbaum, G.; van Ormondt, M. Seasonal-scale nearshore morphological evolution: Field observations and numerical modeling. *Coast. Eng.* **2009**, *56*, 1153–1172. [[CrossRef](#)]
82. Gallagher, E.L.; Elgar, S.; Guza, R.T. Observations of sand bar evolution on a natural beach. *J. Geophys. Res.* **1998**, *103*, 3203–3215. [[CrossRef](#)]
83. Masselink, G.; Pattiaratchi, C.B. Seasonal changes in beach morphology along the sheltered coastline of Perth, Western Australia. *Mar. Geol.* **2001**, *172*, 243–263. [[CrossRef](#)]
84. Quartel, S.; Kroon, A.; Ruessink, B.G. Seasonal accretion and erosion patterns of a microtidal sandy beach. *Mar. Geol.* **2008**, *250*, 19–33. [[CrossRef](#)]
85. Nordstrom, K.F. *Estuarine Beaches: An Introduction to Physical and Human Factors Affecting Use and Management of Beaches in Estuaries, Lagoons, Bays and Fjords*; Elsevier Applied Science: London, UK, 1992; p. 217.
86. Jiang, S.; Dickey, T.D.; Steinberg, D.K.; Madin, L.P. Temporal variability of zooplankton biomass from ADCP backscatter time series data at the Bermuda Testbed Mooring site. *Deep-Sea Res. Part I Oceanogr. Res. Pap.* **2007**, *54*, 608–636. [[CrossRef](#)]
87. Ghaffari, P.; Azizpour, J.; Noranian, M.; Chegini, V.; Tavakoli, V.; Shah-Hosseini, M. Estimating suspended sediment concentrations using a broadband ADCP in Mahshahr tidal channel. *Ocean Sci. Discuss.* **2011**, *8*, 1601–1630.
88. Nortek. Welcome to the Nortek Support Center. Available online: <https://support.nortekgroup.com/hc/en-us/categories/360001447411-Manuals> (accessed on 15 September 2022).

89. Gartner, J.W.; Cheng, R.T.; Wang, P.-F.; Richter, K. Laboratory and field evaluations of the LISST- 100 instrument for suspended particle size determinations. *Mar. Geol.* **2001**, *175*, 199–219. [[CrossRef](#)]
90. Thorne, P.D.; Vincent, C.E.; Hardcastle, P.J.; Rehman, S.; Pearson, N. Measuring suspended sediment concentration using acoustic backscatter devices. *Mar. Geol.* **1991**, *98*, 7–16. [[CrossRef](#)]

**Disclaimer/Publisher’s Note:** The statements, opinions and data contained in all publications are solely those of the individual author(s) and contributor(s) and not of MDPI and/or the editor(s). MDPI and/or the editor(s) disclaim responsibility for any injury to people or property resulting from any ideas, methods, instructions or products referred to in the content.